Robust estimation of VTI (vertical symmetry axis) models via joint migration inversion Including multiples in anisotropic parameter estimation

Verschuur, D.J.; Alshuhail, A.A.

DOI
10.1190/geo2017-0856.1

Publication date
2018

Document Version
Final published version

Published in
Geophysics

GEOPHYSICS®

Robust Estimation of VTI models via Joint Migration Inversion: Including multiples in anisotropic parameter estimation

Journal:	*Geophysics*
Manuscript ID	GEO-2017-0856.R1
Manuscript Type:	Technical Paper
Keywords:	anisotropy, multiples, VTI, full-waveform inversion
Area of Expertise:	Anisotropy, Seismic Inversion

Robust Estimation of VTI models via Joint Migration Inversion: Including multiples in anisotropic parameter estimation

Abdulrahman A. Alshuhail[1] **and D.J. Verschuur**[2]

[1]*Saudi Aramco,*

Dhahran,

Saudi Arabia,

E-mail: abdulrahman.shuhail@aramco.com

[2]*Delft University of Technology,*

Lorentzweg 1,

Delft,

E-mail: D.J.Verschuur@tudelft.nl

(October 16, 2018)

Manuscript

Running head: **Anisotropic Joint Migration Inversion**

ABSTRACT

ABSTRACT

Since the Earth is predominately anisotropic, the anisotropy of the medium needs to be included in seismic imaging to avoid mispositioning of reflectors and unfocused images. Deriving accurate anisotropic velocities from the seismic reflection measurements is a highly nonlinear and ambiguous process. To mitigate the nonlinearity and trade-offs between parameters, we propose to include anisotropy in the so-called Joint Migration Inversion (JMI) method, where we limit ourselves to the case of transverse isotropy with a vertical symmetry axis (VTI). The JMI method is based on strictly separating the scattering effects in the data from the propagation effects. The scattering information is encoded in the reflectivity operators, while the phase information is encoded in the propagation operators. This strict separation enables the method to be more robust, in that it can appropriately handle a wide range of starting models, even when the difference in traveltimes are more than a half cycle away. The method also utilizes internal multiples in estimating both the reflectivities and the anisotropic velocities. Including internal multiples in inversion not only reduces the cross-talk in the final image but can also reduce the trade-off between the anisotropic parameters, since internal multiples usually have more of an imprint of the subsurface parameters compared to primaries. The inverse problem is parametrized in terms of a reflectivity, vertical velocity, horizontal velocity, and a fixed δ value. The method is demonstrated on a number of synthetic models and a marine dataset from the North Sea. Results show that utilizing JMI for anisotropic inversion makes the inversion robust in terms of using highly erroneous initial models. Moreover, internal multiples can contain valuable information on the subsurface parameters, which can help to reduce the trade-off between anisotropic parameters in inversion.

INTRODUCTION

The need to incorporate seismic anisotropy in the imaging process has been clearly demonstrated in the past few decades (Alkhalifah and Tsvankin, 1995; Anderson et al., 1996; Han et al., 2000). Properly accounting for the true propagation effects produces more accurate reflector depths and a better-focused image. Therefore, estimating the anisotropic parameters is essential to arrive at an accurate image. The nonlinear and nonorthogonal multiparameter nature of anisotropic parameter inversion creates a huge challenge (Tsvankin et al., 2010; Plessix and Perkins, 2010; Gholami et al., 2013a; Alkhalifah, 2014; Alkhalifah and Plessix, 2014).

Traditionally, the anisotropic model is estimated as a separate step from imaging, where semblance analysis is done to pick the effective anisotropic parameters (Alkhalifah, 1997; Robein, 2003). This approach is useful for simple layered geology. For dipping structures with strong lateral velocity variations this approach may neither be appropriate nor sufficient to estimate the anisotropic parameters.

Methods that utilize the imaging process to estimate velocities (Al-Yahya, 1989; Symes and Carazzone, 1991; Symes and Kern, 1994) such as Migration Velocity Analysis (MVA) are more suitable for complex geologic structures since they can take into account lateral velocity changes. MVA methods have been generalized to take into account anisotropic kinematics (Li and Biondi, 2011; Weibull and Arntsen, 2014; Li et al., 2017). Despite the improved image quality, the main limitation of MVA still holds in that the linearization of the Born series limits the method to single-scattering reflection data. Therefore, multiples are considered as noise.

Recently, we have seen a shift in the industry to use waveforms to automatically es-

timate the velocities, a popular example is Full Waveform Inversion (FWI) (Tarantola, 1987; Virieux and Operto, 2009). FWI methods are able to invert for the long-wavelength (smooth) components of the velocity as well as the short-wavelength (sharp) components. The long-wavelength component is encoded in the kinematic part of the wavefield. The short-wavelength (high resolution) component is encoded in the amplitudes of the wavefield. Separation of the long- and short-wavelengths is not easily achievable in traditional FWI, consequently the method suffers from a high degree of nonlinearity. Updating the long-wavelengths is seldom achieved, since sufficiently low-frequencies are usually not recorded in the data (Bunks et al., 1995). Diving waves need to be recorded at very large offsets to update the deeper parts of the model (Pratt, 1999). Many authors incorporate anisotropic parameter estimation in the FWI scheme (Plessix and Perkins, 2010; Lee et al., 2010; Gholami et al., 2013a; Alkhalifah, 2014; Alkhalifah and Plessix, 2014; Cheng et al., 2014). As in the isotropic version of FWI, the high degree of nonlinearity and the need to acquire low frequencies and far offsets limits its application.

A fourth strategy, that we consider in this paper, is Joint Migration Inversion (JMI). It was originally proposed by Berkhout (2012, 2014c) and implemented by Staal and Verschuur (2012, 2013). In this method, the reflectivity and velocities are inverted in a full waveform approach, such that both the dynamics and kinematics of the data are taken into account. The approach is based on parameterizing the modeling and inversion in terms of scattering and propagation operators, which can be translated into reflectivities and velocities, respectively. The process consists of two operations that are done sequentially, estimating the reflectivities and then updating the velocities. The reflectivities are estimated through Full Wavefield Migration (FWM) (Berkhout, 2014b; Davydenko and Verschuur, 2017b), while the tomographic component is presented in Berkhout (2014c). Both parts utilize recursive

one-way operators to propagate both the source and receiver wavefields along the depth axis.

Perhaps the most significant and unique property of JMI is that this strict separation, of the scattering and propagation, enables the JMI method to decrease the degree of nonlinearity and, in turn, mitigates the effect of cycle skipping (Staal et al., 2014; Alshuhail and Verschuur, 2015; Berkhout et al., 2015; Verschuur et al., 2016). It provides an integrated solution in that it provides the image and the model. There is no need to apply imaging after obtaining the model, such as in MVA and FWI.

JMI utilizes all types and orders of multiples, both surface and internal multiples, without having to define any multiple generating surfaces. The estimated image automatically provides the multiple generating structures that scatter the multiple energy. Note that this type of recursive modeling of scattered energy is akin to the so called Bremmer series (Bremmer, 1951; Wapenaar, 1996; de Hoop et al., 2000). Multiples generally spend more time in the subsurface, compared to primaries; therefore, have a higher vertical resolution of the subsurface parameters (Zhang and Schuster, 2013; Berkhout, 2014c; Berkhout and Verschuur, 2016). Using them also broadens the subsurface illumination and attenuates the effect of shadow zones (Alkhalifah and Wu, 2016; Davydenko and Verschuur, 2017b), therefore providing a more balanced illumination of the subsurface (Whitmore et al., 2010; Kumar et al., 2014; Lu et al., 2015). A unique benefit of using internal multiples is that it enables imaging structures from below as shown by Davydenko and Verschuur (2013, 2017b). Finally, since the multiples are naturally explained in the forward model for JMI, their cross-talk is automatically attenuated (Berkhout, 2014b; Davydenko and Verschuur, 2017b). By utilizing the joint inversion of reflectivity and velocity and including all multiples in a full waveform, data-driven way, JMI is able to produce a sharp reflectivity model

and a smooth, but accurate, velocity model of the subsurface.

In its current implementation JMI assumes the subsurface to be isotropic. In reality there are many areas where anisotropy is significant (Byun et al., 1989; Lynn et al., 1991), and ignoring anisotropy leads to poor results. In this paper, we consider Vertical Transverse Isotropic (VTI) examples. VTI media can be defined as media that have a vertical axis of symmetry, where the medium is invariant to any rotation around this axis. This is the case for thinly bedded sedimentary sequences and for horizontally bedded shales (Levin, 1979; Banik, 1984). P-wave kinematics (for depth imaging) in VTI media can be described by the P-wave velocity along the vertical symmetry axis V_v and the so-called Thomsen parameters δ and ϵ (Thomsen, 1986). Alternatively, one can use a combination of the following identities with the previous parameters to describe VTI kinematics, the NMO velocity given by $V_{nmo} = V_v\sqrt{1+2\delta}$, the horizontal velocity given by $V_h = V_v\sqrt{1+2\epsilon}$, and the anellipticity given by $\eta = \frac{\epsilon-\delta}{1+2\delta}$ (Alkhalifah and Tsvankin, 1995).

With various parameterizations available for VTI inversion, choosing the optimal one for inversion is not straightforward. Many authors analyze different parameterizations for inversion (Plessix and Cao, 2010; Gholami et al., 2013b; Alkhalifah, 2014; Alkhalifah and Plessix, 2014) and we rely on their work to understand the advantages and disadvantages of the different parameterizations. We find that a V_v, δ, and V_h parameterization is ideal for our VTI implementation of JMI. It minimizes the trade-off between the parameters, where the narrow wavenumber content updates the V_v parameter and the wide wavenumber content updates the V_h parameter. It also avoids scaling issues, since the inverted parameters are at the same scale. Note that δ is often called the depthing parameter, because it ties V_v to V_{nmo}. δ suffers from intrinsic ambiguity between it and depth, as shown in Alkhalifah and Tsvankin (1995) and later in Plessix and Cao (2010). Due to the intrinsic ambiguity we

will not estimate δ from surface seismic data; instead it will be derived from other sources of information, such as well logs.

In this paper, we explore the possibility of incorporating VTI kinematics in the JMI scheme, to make JMI better applicable in realistic geologic settings. We present a data-domain inversion-based imaging and anisotropic velocity analysis approach that uses primary reflections as well as multiple reflections, without any a priori knowledge of the multiple-generating boundaries. The method is flexible in that inaccurate starting models can be handled, where the strict separation of the reflectivity from the anisotropic velocity models promotes this flexibility. The method is relatively hands off in terms of user interference once the initial setup is defined.

The remainder of this paper consists of seven sections. The first section of this paper presents the VTI extension to JMI's modeling engine, Full Wavefield Modeling (FWMod). In the second section we analyze the cost function behavior for a number of different scenarios. The third section presents the theoretical framework and the derivation of the gradients for anisotropic JMI. We follow it up with the fourth section were we illustrate the capabilities of anisotropic JMI on different synthetic models. The fifth section demonstrates the application of the method on a marine dataset from the North Sea. Finally, the discussion and conclusions are given.

FORWARD MODELING: ANISOTROPIC FWMOD

Full Wavefield Modeling (FWMod) is an integral based approach that models reflection-type events (Berkhout, 2012, 2014a; Davydenko and Verschuur, 2013, 2017b). It explains the seismic reflection response in terms of two independent operators per depth level, a

scattering operator denoted by $\mathbf{R}$, and a local propagation operator denoted by $\mathbf{W}$. $\mathbf{R}$ contains the reflection information of the subsurface while the kinematics of wave propagation (anisotropic velocity) is encoded in the $\mathbf{W}$ operators. Using $\mathbf{R}$ and $\mathbf{W}$ we can model primary, internal multiple, and surface-related multiple reflections. It consists of two main operations that are done sequentially, scattering and extrapolation. Note that the vector and matrix notation used in this paper is the same notation introduced by Berkhout (1980). It describes wavefields as a function of space for one frequency component as a vector.

Scattering

Assume a set of scatterers in the subsurface along a depth level z_m (Figure 1). That depth level can have two wavefields approaching it, namely a downgoing wavefield, represented by $\vec{P}^+(z_m; z_s)$, and an upgoing wavefield, represented by $\vec{P}^-(z_m; z_s)$, where z_s refers to the location of the source that created these wavefields. The outgoing wavefields just above, represented by $\vec{Q}^-(z_m; z_s)$, and below, represented by $\vec{Q}^+(z_m; z_s)$, are given by:

$$\vec{Q}^-(z_m; z_s) = \vec{P}^-(z_m; z_s) + \delta\vec{S}(z_m; z_s) \tag{1}$$

$$\vec{Q}^+(z_m; z_s) = \vec{P}^+(z_m; z_s) + \delta\vec{S}(z_m; z_s)\ , \tag{2}$$

where

$$\delta\vec{S}(z_m; z_s) = \mathbf{R}^{\cup}(z_m)\vec{P}^+(z_m; z_s) + \mathbf{R}^{\cap}(z_m)\vec{P}^-(z_m; z_s), \tag{3}$$

with $\delta\vec{S}$ being defined as the secondary sources along the depth level z_m. In these equations $\mathbf{R}^{\cup}$ and $\mathbf{R}^{\cap}$ are the reflectivity operators acting from above and below, respectively.

In this formulation the reflectivity $\mathbf{R}$ can be parametrized as angle-independent or angle-dependent. For the angle-independent case the reflectivity matrix $\mathbf{R}$ is a diagonal matrix with scalar coefficients. For this paper the reflectivity is assumed to be angle-independent as we will focus on velocity estimation. For the 2D case this means that the angle-independent reflectivity is given as ($i = 1, 2, ..., I$):

$$\mathbf{R}^{\cup}(z_m) = diag\left(R(x_1, z_m), R(x_2, z_m), ..., R(x_i, z_m), ...R(x_I, z_m)\right), \tag{4}$$

with $R(x_i, z_m)$ being the angle-independent reflectivity value at x_i and depth level z_m. The angle-independent reflectivities will only provide structural knowledge of the subsurface.

Extrapolation

Extrapolating the outgoing wavefields $\vec{Q}^{-}(z_m; z_s)$ and $\vec{Q}^{+}(z_m; z_s)$ to the next scattering depth level is done via the operator $\mathbf{W}$. $\mathbf{W}$ is a forward propagation operator. Each column is associated with the derivative of Green's function dictating wave propagation from one depth level to the next. For the 2D isotropic homogeneous case the scalar expression can be defined as (Berkhout, 1980; Wapenaar and Berkhout, 1989):

$$\vec{W}(z_{m+1}, z_m) = \mathcal{F}_x^{-1}\left[e^{-jk_z\Delta z}e^{-jk_x s_i}\right], \tag{5}$$

where $\Delta z = |z_{m+1} - z_m|$, k_z is the vertical wavenumber, k_x is the horizontal wavenumber, s_i is the source position of the Green's function, and $\mathcal{F}_x^{-1}$ indicates taking the inverse spatial Fourier transform and organizes the result in a vector. For the isotropic case k_z can be written as:

$$k_z = \sqrt{\frac{\omega^2}{v^2} - k_x^2} \tag{6}$$

where v is the local propagation velocity and ω is the angular frequency. Anisotropic wave propagation for VTI media can be easily incorporated by redefining k_z. The acoustic anisotropic dispersion relation can be utilized in order to include the P-wave VTI kinematics (Alkhalifah, 2000a). It is given as:

$$k_z^2 = \frac{V_{nmo}^2}{V_v^2}\left(\frac{\omega^2}{V_{nmo}^2} - \frac{\omega^2 k_x^2}{\omega^2 - 2V_{nmo}^2\eta k_x^2}\right) , \tag{7}$$

It is possible to rewrite the dispersion equation in terms of V_v, δ, and V_h as:

$$k_z^2 = \frac{\omega^2}{V_v^2} - \left(\frac{\omega^2(1+2\delta)k_x^2}{\omega^2 - V_h^2 k_x^2 + V_v^2(1+2\delta)k_x^2}\right) . \tag{8}$$

The acoustic anisotropic dispersion relation has limitations if we convert it directly to a wave equation. Two limitations were documented by Alkhalifah (2000a) when deriving the anisotropic acoustic wave-equation. The first one was a pseudo S-wave (diamond shaped shear wave mode) that occurred if the source or receivers were in or near anisotropic media. The second limitation was an exponentially increasing solution for negative values of η. These limitations can be attenuated in a straightforward manner using a phase-shift extrapolation approach (Alkhalifah, 2000b; Bale, 2007; Alshuhail and Verschuur, 2014). The pseudo S-wave can be directly distinguished and eliminated in the phase shift operator. The exponentially growing solution for negative η can be ensured to decay by having control of the sign of the exponent of the phase shift operator.

We base our modeling engine on an acoustic anisotropic approximation of the subsurface, although its validity is questionable when comparing it with real elastic data. Full elastic modeling requires much more parameters and subsequently more parameters to invert for. Therefore, an accurate starting model is essential for inversion to avoid the null

space. Starting with an acoustic approximation can help identify and estimate the essential parameters for subsequent inversion. Three or sometimes four component data is required for elastic inversion. Frequently, single component pressure or vertical displacement data is all that is recorded. Therefore, in this paper, we assume that the data we are dealing with mainly consists of P-wave arrivals. We also assume that the contrasts are relatively weak. Therefore, the S-wave and converted waves are weak. If the elastic effects are prominent we will rely on preprocessing that mitigates the elastic effects.

Combining the scattering and extrapolation operations, we arrive at the governing equations for FWMod (Berkhout, 2014a). For downgoing wavefields ($m = 1, 2, ..., M$):

$$\vec{P}^{+}(z_m; z_0) = \mathbf{W}^{+}(z_m, z_0)\vec{S}(z_0) + \sum_{k=0}^{m-1} \mathbf{W}^{+}(z_m, z_k)\delta\vec{S}(z_k; z_0), \tag{9}$$

for upgoing wavefields ($m = 0, 1, ..., M-1$):

$$\vec{P}^{-}(z_m; z_0) = \mathbf{W}^{-}(z_m, z_M)\vec{P}^{-}(z_M; z_0) + \sum_{k=m+1}^{M} \mathbf{W}^{-}(z_m, z_k)\delta\vec{S}(z_k; z_0). \tag{10}$$

$\vec{S}(z_0)$ represents the source wavefield generated at the surface level. Note that $\mathbf{W}^{+}$ and $\mathbf{W}^{-}$ are the downgoing and upgoing VTI one-way scatter free-operators, respectively. The modeling is done iteratively in so-called roundtrips. Each roundtrip adds an order of scattering by updating the scattering wavefields $\delta\vec{S}$, according to Equation 3. Therefore, for the first roundtrip only primaries without transmission effects are modeled. For the second roundtrip, primaries and first-order multiples are modeled and so on for subsequent roundtrips. With more roundtrips the transmission effects become more accurate. The recursive modeling method is based on the Bremmer series (Bremmer, 1951; Wapenaar, 1996; de Hoop et al., 2000), where each iteration adds a new order of scattering. Note that in this description we do not take into account diving waves nor do we consider surface waves

such as direct waves and ground roll. The recorded data is assumed to consist of upgoing wavefields only, and so for the marine datacase deghosting must be done prior to inversion.

COST FUNCTION ANALYSIS

The cost function is analyzed to understand the nonlinearity associated with the chosen parametrization (V_v, V_h, and δ). We consider a simple $2000m$ wide by $650m$ deep model with an anomaly in the middle (Figure 2a). The anomaly has a vertical velocity of $V_v = 3300m/s$ and a horizontal velocity of $V_h = 3905m/s$, which corresponds to an ϵ of 0.2. δ was set to zero in this example. There are two prominent reflectors at the top and bottom of the anomaly. There are 41 sources located at equal intervals at the surface. Receivers are also located at the surface at $20m$ intervals. A dense source and receiver acquisition geometry is used to reduce the effect of extending the illumination caused by the multiples. The misfit function is evaluated over different values of V_v and V_h. The misfit function is given as:

$$J = \sum_{shots} \sum_{\omega} \left\| \vec{P}^{-}_{obs}(z_0) - \vec{P}^{-}_{mod}(z_0) \right\|^2 = \sum_{shots} \sum_{\omega} \left\| \vec{E}^{-}(z_0) \right\|^2 , \tag{11}$$

where $\vec{P}^{-}_{obs}(z_0)$ represents the monochromatic component of the observed or measured wavefield at the surface and $\vec{P}^{-}_{mod}(z_0)$ is the monochromatic component of the modeled or calculated wavefield at the surface z_0. Note that in this example no direct waves were considered, only upgoing reflections were recorded (i.e., deghosted data). The misfit function is analyzed by evaluating different sets of vertical and horizontal velocities.

For the first example we do not estimate the reflectivity, but rather fix it to the correct value and position and evaluate the cost function over different sets of vertical and horizontal velocities. In this example, only the primaries are modeled. Figure 2b shows the associated

misfit function. The V_v parameter is very well defined compared to V_h, as there is no vertical valley. There is a large horizontal valley along the V_h parameter. Perhaps the most prominent issue that is apparent are the local minima that are caused by so-called cycle skipping. When the reflectivity is fixed and not updated, the reflected events in the data might appear more than half a cycle away from each other (depending on the trial velocities), and therefore a meaningful update is not obtained (Alkhalifah, 2017). Figures 3a-c show this case in the shot domain. Note that the second event in the trial gather arrives very late compared to the true one. The trial velocities, corresponding to $V_v = 2300m/s$ and $V_h = 2905m/s$, cause the second reflection to be more than half a cycle away from the true one. If one were to use gradient decent methods it would be very difficult to converge to the global solution without modifying the inversion technique.

To mitigate the cycle skipping problem we re-evaluate the misfit function, using the same model and the same geometry as in the previous experiment. For each trial point (V_v and V_h pair) the best fit reflectivity is evaluated as well via FWM. Therefore, we do not assume a fixed reflectivity. The reflectivity moves the reflected event to the location that produces the least error between the observed and calculated data. Figure 2c shows the associated misfit function for the second experiment. What is noteworthy is that the local minima are no longer there. By allowing the reflectivity to move, it is possible to drastically reshape the misfit function and enable it to be more suitable for gradient descent methods. Figures 3d-f show shot gathers that correspond to the same shot gathers in Figures 3a-c, however, in this case the best fit reflectivity is estimated. Note that the second reflection in the trial gather falls on top of the second reflection in the observed gather (around the apex). Hence, updating the velocities is more manageable than in the previous case. This is what makes JMI a robust process (Verschuur et al., 2016). Despite the absence of local

minima, there is a trade-off between V_v and V_h (the slanted valley). This trade-off would cause issues in arriving at a unique solution, because many solutions fit the data fairly well. Without a priori information it is difficult to arrive at a unique solution, especially when there is noise present.

One would like to reduce the trade-off as much as possible. Therefore, one obvious way to reduce it is by redesigning the acquisition survey such that more horizontally traveling waves are acquired. This can be done by extending the maximum offset to double its initial value. The receivers span $4000m$ with the same sources as in the previous experiment. Figure 2d shows the new misfit function, where the valley is much narrower in the V_h parameter than in Figure 2c. The reason is because there are more horizontally traveling waves acquired in the data, which help in better defining the horizontal velocities. However, the accuracy of the vertical velocity does not improve much due to the reflector depth and velocity trade-off.

Another way to reduce the trade-off is to include internal multiples in the inversion. Using the original geometry both the observed and modeled data include internal multiples, to understand their effects on the cost function (Figure 2e). Both the vertical velocity and horizontal velocity are more uniquely defined, compared to the primary-only case (Figure 2c versus Figure 2e). Surprisingly, they are also more uniquely defined compared to the third experiment where the offset was doubled (Figure 2d versus Figure 2e). Figures 3g-i show shot gathers that correspond to the same gathers in Figures 3d-f, however, the internal multiples are included and the best fit reflectivity is estimated. In this experiment the multiples are mostly associated with vertical propagation paths. This is because multiples usually have a smaller propagation angle compared to primaries at the same offset. They are more sensitive to V_v. To obtain accurate V_h estimates one must have accurate V_v estimates

for surface seismic geometries. We believe that although the internal multiples are mostly associated with smaller angles than primaries, their influence leaks onto the V_h parameter in an indirect way. The more accurate the V_v estimate, the more accurate the V_h parameter is in turn.

Finally, to evaluate the role of the internal multiples, we compute the cost function corresponding to only internal multiples in the observed and modeled data. Figure 2g shows this cost function, where it should be noted that primaries were still used to build the incident wavefields for the internal multiples, but in the observed data only the mismatch in internal multiples was evaluated. Figures 3j-l show the corresponding shot gathers. We note that the cost function is better constrained than in the primary only case. Note that the relation between the primaries and multiples is non-linear in nature, and therefore, the primary information leaks indirectly to the multiples. For instance the multiple generating boundaries are obtained from the primaries prior to estimating the cost function, therefore, the primary information is still used to build the wavefields for generating the multiples. For example, the multiple generating boundaries are obtained from the primaries prior to estimating the cost function. However, the cost function shows the final effect of the velocity errors on the observed multiples in the data. By employing all the strategies outlined here, one may reduce nonlinearity and trade-off, via estimating the reflectivity separately, choosing a suitable parametrization, opting for a wider acquisition geometry, and taking internal multiples into account.

ANISOTROPIC JMI THEORY

Anisotropic JMI invlolves updating three parameters, namely the angle-independent reflectivities (associated with the $\mathbf{R}$ operator), the vertical velocities, and the horizontal velocities

(the latter two are both associated with the **W** operator). The reflectivities will be obtained via FWM. We follow the same procedure presented in Davydenko and Verschuur (2017b) in order to obtain the angle-independent reflectivities. The remainder of this section will address the V_v and V_h parameters.

Vertical Velocity

We define a vertical velocity contrast parameter β_v as:

$$\beta_v(x,z) = 1 - \frac{V0_v(x,z)^2}{V_v(x,z)^2}, \tag{12}$$

where $V0_v$ is the background vertical velocity, while V_v is the true vertical velocity. The extrapolation operators in the true medium for the upgoing and downgoing wavefields are then defined as:

$$\mathbf{W}^-(z_m, z_{m+1}) = \mathbf{W}_0^-(z_m, z_{m+1}) + \Delta\mathbf{W}^-(z_m, z_{m+1}), \tag{13}$$

and

$$\mathbf{W}^+(z_{m+1}, z_m) = \mathbf{W}_0^+(z_{m+1}, z_m) + \Delta\mathbf{W}^+(z_{m+1}, z_m), \tag{14}$$

where $\mathbf{W}_0^{\mp}$ are the extrapolation operators defined in the background medium and $\Delta\mathbf{W}^{\mp}$ are the differences between the true and background operators. The linearization of a single column of $\Delta\mathbf{W}^{\mp}$ with respect to β_v is given as:

$$\Delta\vec{W}^-(z_m, z_{m+1}) \approx \left[\frac{\partial\vec{W}^-}{\partial\beta_v}\right]_{\beta_v=0} \beta_v(x,z_m) = \vec{G}_v^-(z_m, z_{m+1})\beta_v(x,z_m), \tag{15}$$

and

$$\Delta\vec{W}^{+}\left(z_{m+1},z_{m}\right)\approx\left[\frac{\partial\vec{W}^{+}}{\partial\beta_{v}}\right]_{\beta_{v}=0}\beta_{v}(x,z_{m})=\vec{G}_{v}^{+}(z_{m+1},z_{m})\beta_{v}(x,z_{m}),\tag{16}$$

where the anisotropic $\vec{G}_v$ is given as:

$$\vec{G}_{v}\left(z_{m},z_{n}\right)\approx\mathcal{F}_{x}^{-1}\left[\frac{j\Delta z}{2k_{z}+\sigma}D_{v}e^{-jk_{z}\Delta z}e^{-jk_{x}x_{i}}\right],\tag{17}$$

and $\mathcal{F}_x^{-1}$ indicates taking the inverse spatial Fourier transform. σ is a stabilization term to avoid dividing by zero. D_v is given by:

$$D_{v}=\left(\frac{\omega}{V0_{v}}\right)^{2}-\frac{\omega^{2}V0_{v}^{2}(1+2\delta)^{2}k_{x}^{4}}{\left(\omega^{2}-(V_{h}^{2}-V0_{v}^{2}(1+2\delta))k_{x}^{2}\right)^{2}}.\tag{18}$$

A detailed derivation of the gradient is provided in Appendix A. Upon further investigation we find that D_v is a scaling term that prioritizes the vertically traveling events (events located close to $k_x = 0$) in updating the β_v gradient. We limit the scaling effect of D_v to span the domain of the real part of k_z, since we are mostly interested in the propagating waves. With the linearization at hand, we can define the total vertical velocity contrast gradient $\Delta\vec{\beta}_v$ as a summation of:

$$\Delta\vec{\beta}_{v}(z_{m})=\Delta\vec{\beta}_{v}^{-}(z_{m})+\Delta\vec{\beta}_{v}^{+}(z_{m}),\tag{19}$$

where $\Delta\vec{\beta}_v^{-}(z_m)$ is the contrast gradient using upgoing waves and $\Delta\vec{\beta}_v^{+}(z_m)$ is the contrast gradient using downgoing waves. They are given by:

$$\Delta\vec{\beta_{v}}^{-}(z_{m})=diag\left(\sum_{shots}\sum_{\omega}\left[\mathbf{G}_{v}^{-}(z_{m},z_{m+1})\right]^{H}\vec{E}^{-}(z_{m})\left[\vec{Q}^{-}(z_{m+1})\right]^{H}\right),\tag{20}$$

and

$$\Delta\vec{\beta_v^+}(z_m) = diag\left(\sum_{shots}\sum_{\omega}\left[\mathbf{G}_v^+(z_{m+1},z_m)\right]^H\vec{E}^+(z_{m+1})\left[\vec{Q}^+(z_m)\right]^H\right), \tag{21}$$

with $\vec{E}^-(z_m)$ being the upgoing back-propagated residual and $\vec{E}^+(z_m)$ being the downgoing back-propagated residual obtained via the reflectivity estimate. They are given by:

$$\vec{E}^-(z_m) = \left[\mathbf{W}^-(z_0,z_m)\right]^H\vec{E}^-(z_0), \tag{22}$$

and

$$\vec{E}^+(z_m) = \sum_{n>m}\left[\mathbf{W}^+(z_n,z_m)\right]^H\mathbf{R}^{\cup}(z_n)\vec{E}^-(z_n). \tag{23}$$

The associated perturbation for the vertical velocity contrast can be defined as:

$$\begin{aligned}\Delta\mathbf{P}^-_{\Delta\beta_v}(z_0) = &\sum_{m=1}^{M}\mathbf{W}^-(z_0,z_m)\,\mathbf{G}_v^-(z_m,z_{m+1})\,\Delta\boldsymbol{\beta_v}(z_m)\,\vec{Q}^-(z_{m+1}) + \\ &\sum_{m=1}^{M}\sum_{n>m}^{M}\mathbf{W}^-(z_0,z_n)\mathbf{R}^{\cup}(z_n)\mathbf{W}^+(z_n,z_{m+1})\mathbf{G}_v^+(z_{m+1},z_m)\Delta\boldsymbol{\beta_v}(z_m)\,\vec{Q}^+(z_m),\end{aligned} \tag{24}$$

where $\Delta\boldsymbol{\beta}_v$ is a square matrix with gradients $\Delta\vec{\beta}_v(z_m)$ along its diagonal. Finally, the new vertical velocities will be updated as:

$$V_v^{(i)} = \frac{V_v^{(i-1)}}{\sqrt{1-\alpha_v\Delta\beta_v}}, \tag{25}$$

where i is the iteration number and α_v is the step length. α_v can be estimated via a line search.

Horizontal Velocity

As in the vertical velocity case, we define a contrast parameter associated with the horizontal velocity as:

$$\beta_h(x,z) = 1 - \frac{V0_h(x,z)^2}{V_h(x,z)^2}, \tag{26}$$

where $V0_h$ is the background horizontal velocity, while V_h is the true horizontal velocity. After linearizing $\Delta\mathbf{W}^{\mp}$ (Equations 13 and 14) with respect to β_h, each column can be written as:

$$\Delta\vec{W}^{-}(z_m, z_{m+1}) \approx \left[\frac{\partial\vec{W}^{-}}{\partial\beta_h}\right]_{\beta_h=0} \beta_h(x,z_m) = \vec{G}_h^{-}(z_m, z_{m+1})\beta_h(x,z_m), \tag{27}$$

and

$$\Delta\vec{W}^{+}(z_{m+1}, z_m) \approx \left[\frac{\partial\vec{W}^{+}}{\partial\beta_h}\right]_{\beta_h=0} \beta_h(x,z_m) = \vec{G}_h^{+}(z_{m+1}, z_m)\beta_h(x,z_m). \tag{28}$$

The anisotropic $\vec{G}_h$ is given as:

$$\vec{G}_h(z_m, z_n) \approx \mathcal{F}_x^{-1}\left[\frac{j\Delta z}{2k_z+\sigma} D_h e^{-jk_z\Delta z} e^{-jk_x x_i}\right], \tag{29}$$

where D_h is given by:

$$D_h = \frac{\omega^2 V0_h^2(1+2\delta)k_x^4}{\left(\omega^2 - (V0_h^2 - V_v^2(1+2\delta))k_x^2\right)^2}. \tag{30}$$

A detailed derivation of the gradient is provided in the Appendix A. Similar to D_v, D_h is a scaling parameter. However, D_h prioritizes events traveling horizontally in updating the β_h gradient. We also limit the scaling effect to be bound by the domain of real k_z values,

to avoid boosting evanescent waves. The horizontal velocity contrast gradient $\Delta\vec{\beta}_h$ is then defined as:

$$\Delta\vec{\beta}_h(z_m) = \Delta\vec{\beta}_h^{-}(z_m) + \Delta\vec{\beta}_h^{+}(z_m), \tag{31}$$

which can be written using the following summations:

$$\Delta\vec{\beta_h^{-}}(z_m) = diag\left(\sum_{shots}\sum_{\omega}\left[\mathbf{G}_h^{-}(z_m, z_{m+1})\right]^H \vec{E}^{-}(z_m)\left[\vec{Q}^{-}(z_{m+1})\right]^H\right), \tag{32}$$

and

$$\Delta\vec{\beta_h^{+}}(z_m) = diag\left(\sum_{shots}\sum_{\omega}\left[\mathbf{G}_h^{+}(z_{m+1}, z_m)\right]^H \vec{E}^{+}(z_{m+1})\left[\vec{Q}^{+}(z_m)\right]^H\right), \tag{33}$$

As in the vertical velocity case we can write the associated perturbation for the horizontal velocity contrast as:

$$\begin{aligned}\Delta\mathbf{P}^{-}_{\Delta\beta_h}(z_0) = &\sum_{m=1}^{M}\mathbf{W}^{-}(z_0, z_m)\,\mathbf{G}_h^{-}(z_m, z_{m+1})\,\Delta\boldsymbol{\beta_h}(z_m)\,\vec{Q}^{-}(z_{m+1}) + \\ &\sum_{m=1}^{M}\sum_{n>m}^{M}\mathbf{W}^{-}(z_0, z_n)\mathbf{R}^{\cup}(z_n)\mathbf{W}^{+}(z_n, z_{m+1})\mathbf{G}_h^{+}(z_{m+1}, z_m)\Delta\boldsymbol{\beta_h}(z_m)\,\vec{Q}^{+}(z_m),\end{aligned} \tag{34}$$

where $\Delta\boldsymbol{\beta}_h$ is a square matrix with gradients $\Delta\vec{\beta}_h(z_m)$ along its diagonal. The update for the horizontal velocity is given as:

$$V_h^{(i)} = \frac{V_h^{(i-1)}}{\sqrt{1-\alpha_h\Delta\beta_h}}, \tag{35}$$

where i is the iteration number and α_h is its associated step length.

Isotropic JMI inverts for the reflectivity and velocity sequentially in the same iteration. With the addition of an extra parameter for the VTI case we need to update the inversion

strategy to include the extra parameter. Starting with an initial $\mathbf{R}$ and V_v that are far from their true values will cause highly erroneous V_h updates for the initial iterations. Arriving at a close enough solution for $\mathbf{R}$ and V_v (for the short offsets) greatly facilitates the convergence of the V_h parameter (Plessix and Cao, 2010; Cheng et al., 2014). Therefore, we prefer to employ a hierarchal approach where we invert for $\mathbf{R}$ and V_v initially and only switch to $\mathbf{R}$, V_v, and V_h inversion when we achieve convergence. The hierarchical approach facilitates including the large wavenumber components in V_v. The δ parameter will not be estimated in our approach due to the intrinsic ambiguity between it and depth. Therefore, it will be estimated from other sources of information, such as well logs, where available. In our tests of the method we have noticed that generally the V_h parameter is resolved better than the V_v parameter. We believe the reason is because V_{nmo}, which is the dominant parameter in VTI inversion, is predominantly mapped to V_h. This phenomena is explained extensively in Alkhalifah (2017).

SYNTHETIC EXAMPLES

In this section, we test the effectiveness of JMI on three synthetic VTI models.

Example 1: Homogeneous Anisotropic Model

In this example we test the effectiveness of the method when the initial model has traveltimes that are more than half a cycle away from the observed data. We generate a homogenous VTI model with constant values of $\rho = 2500$, $V_{P0} = 4000m/s$, $\epsilon = 0.2$, $\delta = 0.1$. The model has a density change at $800m$, where the density changes to $\rho = 3000$. Figures 4a, 4b, and 4g show the parameters that we are interested in inverting for, namely the vertical

velocity, the horizontal velocity, and the reflectivity. A total of 150 shots were generated at the surface at equal intervals. The source wavelet is a Ricker wavelet with an average frequency of $20Hz$ as the source wavelet. The receivers span the surface at $20m$ intervals.

Figures 4c and 4d show the starting models. Note that the vertical velocity difference is $800m/s$ over $800m$ and horizontal velocity difference is over $1500m/s$ over the same $800m$ interval. This will create large discrepancies between the reflection arrival times between observed and calculated data sets, which will create issues in inversion if the reflectivity is not estimated at each iteration. Figures 4e, 4f, and 4h show the inverted results. Note that although there is only one reflector, the estimated velocities and the estimated reflectivity are close to their true counterparts. The inverted results are accurate except at the edges due to the poor illumination. It is interesting to note the difference between the edges and the middle of the model. We can see the effect of updating the velocities on the image, comparing the reflector at the edges and the middle of the model we can see that the reflector shifted more than $200m$.

Example 2: Internal Multiple Model

To analyze the effects of internal multiples in inversion, we use a model that generates strong internal multiples. Figure 5 shows the true reflectivity, vertical velocity, horizontal velocity, and δ values. The strong internal multiples are generated by the high reflectivity contrast at the top and base of the second layer (between $160m$ and $350m$). The multiples mask weaker primaries that are generated below $350m$. A total of 151 shots were used at the surface at equal intervals. The source wavelet is a Ricker wavelet with a peak frequency of $30Hz$. The receivers span the $3000m$ section at $20m$ intervals.

The initial reflectivity was set to zero, while the initial velocity models are 1D linear models that range from 2120 to $2370m/s$ for V_v and 2315 to $2530m/s$ for V_h. As in the previous case we initially only invert for $\mathbf{R}$ and V_v until convergence and then include V_h inversion. Figure 6a, 6b, and 6c show the inverted results. Figures 6d and 6e show the log profiles at the middle of the model. As expected, the estimated velocity models are a smooth version of their true counterparts. Note that the results degrade at the edges of the model due to the limited illumination in those areas.

Next, we repeat the inversion using the same initial models. We limit the inversion to primaries-only. Therefore, internal multiples are present in the observed data, however, they will not be addressed in inversion and will be considered as noise. In this example, the multiples occur through the record and mask weaker primaries. Figure 7 shows the primary-only inversion results. Comparing the primary-only inversion velocities with the full wavefield inversion velocities, we note that velocities in the area below the high velocity layer are overestimated. We believe that this is due to cross-talk between the primaries and internal multiples. Since the internal multiples have larger amplitudes the method prioritizes them in inversion and tries to explain them as primaries, resulting in higher velocities than expected. Consequently, the corresponding image shows (a strong imprint from internal multiples at z=600m in Figure 7a) overlying the primary events.

Finally, we consider the case where only primaries are both modeled and inverted. There are no internal multiples in the observed data, i.e., we assume that they were perfectly removed and will not have any contribution in the inversion. We recompute the observed data and limit it to a single roundtrip of FWMod to model the primaries-only.

We then start the inversion with the same set of starting parameters as in the previous

examples. Figure 8 shows the inverted results. It appears that a trade-off is apparent in the inverted results, where the vertical velocity is overestimated while the horizontal velocity is underestimated compared to Figure 6. We calculate the mean percentage difference between the true velocities and all inverted velocities for the different cases, Table 1 shows the results. We find that the error is the least when primaries and multiples are included and inverted. This suggests that the internal multiples added the extra sensitivity in both the velocity estimates, similar to the effect that was shown in the cost function analysis (Figure 2e). Note that the image in Figure 8 suffers due to the trade-off, the mean percentage error is larger than in Figure 6. Despite the absence of internal multiples in the observed data, the inverted results are of lower quality. This result shows that the internal multiples (even in the case of dense data sampling) can contribute in the velocity estimation process.

Example 3: HESS VTI Model

We validate our theory on the so-called Hess VTI model. This model was generated in the late 1990s by the Amerada Hess Corp to be representative of several exploration areas in the Gulf of Mexico. We consider only part of the model containing the fault, we also subsample and rescale the model due to its large size.

Figure 9 shows the true reflectivity, vertical velocity, horizontal velocity, and δ models. The acquisition configuration is a fixed spread survey with 87 equally spaced shots at the surface, the receivers are also located at the surface at $20m$ intervals. We use a $30Hz$ Ricker wavelet as the source waveform. Note that the minimum frequency used in the inversion is $5Hz$ while the maximum frequency used is $80Hz$, with all other frequencies zeroed out.

The initial reflectivity was set to zero, while the initial velocity models are 1D vertically

varying models that increase linearly from 1500 to $4200m/s$ for V_v and 1500 to $4600m/s$ for V_h (Figure 10). We first invert for the reflectivity and vertical velocity before including the horizontal velocity estimation after we achieve convergence. Figure 11 shows the final inverted results. As expected, the image is band-limited but corresponds well to the true image, whereas the velocities are a smooth version of their true counterparts. Note that internal multiples were addressed in the inversion method, as they no longer appear as significant artifacts in the image or the velocities. The fault is reasonably well represented in both velocity models.

APPLICATION TO MARINE DATA

This section illustrates the application of anisotropic JMI on a 2D marine field data set from the North Sea. Our aim is to automatically estimate the reflectivities, vertical velocities, and horizontal velocities of the subsurface.

The seismic reflection data that we invert is 2D streamer data that was acquired from the North Viking Graben in the North Sea (Keys and Foster, 1998). The data is publicly available (courtesy of the SEG and ExxonMobil). Note that the presence of anisotropy, mainly due to thin layering, is well-known in the North Sea (Banik, 1984). The data consists of 1001 shots with a shot spacing of $25m$. The receiver spacing is also $25m$. The recording time is $6s$ and the sampling time is $0.004s$. The acquisition geometry is an off-end spread with a minimum offset of $262m$ and a maximum offset of $3237m$. We make use of reciprocity to transform the off-end geometry to a split-spread geometry. We generate missing near offsets via Radon interpolation (Kabir and Verschuur, 1995). In our formulation we assume that the recorded data consists of upgoing waves only, therefore, we deghost the data. Finally, due to the large size of the data we consider a $4km$ subsection, consisting of 161

shots. To get a general idea of the geology in the region we generate a zero-offset section (Figure 12). The shallow layers are flat while the deeper layers are gently dipping. We believe that a VTI model can be considered since most of the events are flat. Note that many of the deeper events are discontinuous and are of lower quality than the shallower events.

The next step lies in estimating a suitable source wavelet for inversion. We applied Estimation of Primaries by Sparse Inversion (EPSI) to estimate the best fit source wavelet (Groenestijn and Verschuur, 2009a,b). We do not require a subsurface model at this stage since EPSI is a fully data-driven method. The surface-related multiples are attenuated via SRME (Verschuur et al., 1992; Verschuur, 2006). Therefore, JMI will focus on inverting the primaries and internal multiples.

A vertical well is located at approximately the middle of the section (indicated by the drilling rig in Figure 12). V_p, V_s, and ρ log measurements were acquired starting at $1000m$ depth. Therefore, the vertical velocities are quite accurate below $1000m$ depth at the well location. The velocities above $1000m$ are relatively unknown.

The initial isotropic velocity model for inversion is a 1D model that was generated by setting the water velocity to $1450m/s$ while the rest of the upper $1000m$ is set to a constant value of $1700m/s$. Finally, we smooth the V_p velocities obtained from the well to fill the region below $1000m$. The initial isotropic model is shown in Figure 13a. We migrate the data (via FWM) using the initial velocity model. Figure 13b shows the resulting FWM image. Note that many of the reflectors are discontinuous and are unfocused. We also generate the corresponding Angle-Domain Common Image Gathers (ADCIGs) to analyze the accuracy of the starting model. Figure 14 shows the ADCIGs for the initial model.

Note that many of the events are curved upwards (indicating a too slow velocity). Also note that the deeper events, below $1000m$ are also curved although their velocities were obtained from well-logs. This may indicate erroneous overburden velocities or the presence of VTI anisotropy.

We apply anisotropic JMI given the isotropic initial model in Figure 13. We follow the same methodology presented in the synthetic examples. In total we run approximately 160 iterations of anisotropic JMI that include frequency bands that range from $2Hz$ to $40Hz$. In this example δ was set to zero, as there was no a priori information about it. Figure 15 shows the estimated vertical velocity, horizontal velocity and resulting reflectivity. Comparing the FWM image in Figure 15c with the initial image in Figure 13b, we find an improvement in the continuity and focusing of the reflectors (e.g., at approximately $800m$). Also note that the two faults are more clearly visible in the deep part of the section.

Figure 16 shows the associated ADCIGs obtained via conventional anisotropic depth migration with our estimated model. Note that the ADCIGs are fairly flat (but not perfect), indicating a suitable model. Note that some of the non-flat events in the ADCIGs can also be attributed to 3D (out-of-plane) effects. Also, the ADCIGs are computed after anisotropic JMI to analyze the accuracy of inversion. They are not utilized in inversion, like in MVA.

Figure 17 shows the observed and modeled data after anisotropic JMI. Note that most of the main reflections are explained. It is interesting to analyze the events that were not explained. Chief among them is a refracted wave (indicated by the arrows). The modeling method FWMod does not take refractions into account, therefore, they are ignored during inversion. Angle-dependent reflectivities and converted waves are also not explained by the method and thus they do not appear in the calculated data. Although we use an acoustic

assumption, it adequately explains many of the events in this dataset.

We take advantage of the imaging engine to examine different orders of scattering, such as primaries-only or primaries and internal multiples. We consider primaries-only imaging, where we limit FWM to Primary Wavefield Migration (PWM) (Berkhout, 2014b; Davydenko and Verschuur, 2017b). The method will explain the primaries, but will not properly explain the internal multiples, such that they will be treated as primaries, yielding cross-talk in the final image. Figure 18a shows the image after applying PWM. More events are imaged in the PWM compared to the FWM image in Figure 15c. We compute the difference between FWM and PWM to show the extra events that were attenuated (Figure 18b). Another interesting observation is that in FWM transmission effects are properly handled, however, the PWM image sufferers from inaccuracies in handling transmission effects. This explains an overall imprint from strong reflectors in the difference plot.

DISCUSSION

JMI relies on all types of reflections (primaries and multiples) to explain the subsurface parameters. Other modes (such as surface waves, diving waves, and mode conversions) occur in the subsurface. These events could provide additional information on the subsurface parameters. Diving waves in particular could help in better defining the horizontal velocity since they travel mostly in a horizontal sense. FWI implementations actually make use of diving waves to update the velocities with great success (Gholami et al., 2013b; Alkhalifah, 2016). When including diving waves in inversion, one must first update the modeling engine to include diving waves. Davydenko and Verschuur (2013) and Berkhout (2014b) introduce an omni-directional implementation of FWMod where they include horizontally traveling waves. It is an initial step that incorporates more of the recorded data. Since diving waves

have a significant part traveling in both an up and down sense and in a left and right sense, it was not yet fully resolved how these different propagation directions interact with each other, while maintaining conservation of energy.

In our implementation we assume that $\mathbf{R}$ is angle-independent, and we therefore discard the off-diagonal elements of the $\mathbf{R}$ matrix. The off-diagonal components in the reflectivity operator can be considered as subsurface offsets of the reflectivity and are routinely used for Amplitude Versus Offset (AVO) or Amplitude Versus Ray-Parameter (AVP) studies. AVO/AVP analysis can shed light on the density, porosity, and even fluid content (Aki and Richards, 1980). The off-diagonal components will also introduce more physics in inversion. Hence, the seismic reflection data will be better explained. For FWM implementations, Davydenko and Verschuur (2017b) show that angle-dependent reflectivities can be estimated by making use of the linear Radon domain. The linear Radon domain transformation allows the off-diagonal components of the reflectivity matrix to map into angle gathers, after which they sum over frequencies. Mapping to the linear Radon domain and summing over frequencies facilitates a more compact representation that avoids over-parameterizing the problem. Extending this towards a JMI application, where the velocity model is estimated along with the angle-dependent reflectivity is not straightforward. One can run the risk of over-parameterizing the problem, such that the angle-dependent reflectivities leak into the velocity estimates and vice versa. Additional constraints, such as flattening CIGs, are being investigated in order to minimize this trade-off (Davydenko and Verschuur, 2017a).

As in all anisotropic inversion techniques the choice of parameterization is critical in obtaining an accurate solution and the trade-off between the different parameters must be taken into account. Although we did not meticulously test the different parameterizations, we based our parameterizations on previous work (Plessix and Cao, 2010; Gholami et al.,

2013b; Alkhalifah, 2014; Alkhalifah and Plessix, 2014). We have chosen a V_v, V_h, and δ parametrization, with δ being excluded from inversion due to the intrinsic ambiguity between it and depth. δ is estimated from other sources of information such as well logs and we focus on the kinematic part of the inversion between V_v and V_h. For our implementation we believe that this choice of parameters minimizes the trade-off between the parameters as much as possible, although more research needs to be conducted in order to put more quantitative conclusions on this issue. One can chose a different parameterization that consists of different combinations of velocities, Thomson parameters, and η. Translating the new parameterization is relatively straightforward. One must re-derive the gradients and apply scaling when combining velocities with unitless parameters (Thomsen parameters and η).

The current implementation of the method is limited to the 2D case. In the case of an area with 3D structures, inaccuracies would build up in the image due to out-of-plane reflections. A 3D application would increase the amount of information and accuracy of the image and the model. Conceptually, the 3D extension of the 2D theory should follow a path similar to the JMI's isotropic 3D extension presented by Marhfoul and Verschuur (2016). In practice, the challenge lies in addressing the sparse and irregular sampling that is common with 3D surveys. However, surface-related multiples can be used as secondary sources in order to fill gaps in the illumination, as was shown by Kumar et al. (2014) and Davydenko and Verschuur (2017b).

In our approach, we linearize the propagation operator $\mathbf{W}$ in terms of a vertical velocity V_v and a horizontal velocity V_h. In doing so we greatly reduce the number of parameters being estimated for each iteration, but we limit ourselves in terms of an anisotropic model and we are prone to parameter trade-off during inversion. Directly estimating the

propagation operator **W**, allows the data, however complex it may be, to be explained by the operator (Berkhout, 2014c). It avoids defining a certain propagation model that the data should obey. In most anisotropic inversion methods the model needs to be set before inversion (VTI, TTI, etc.). If parts of the model do not obey this assumed model then there will be errors in inversion. An operator description of the subsurface does not impose any anisotropic models. The data is explained by the operators, with fully flexible phase functions, which increases the applicability of the method to a wider range of anisotropic models. The other advantage lies in that the trade-off between the anisotropic parameters in inversion is no longer an issue. The inverted operator will be estimated such that it explains the reflection data. In this approach parameterization in terms of more traditional anisotropic parameters is postponed to the end of inversion when the most accurate operator is estimated.

Although inverting directly for the propagation operator **W** addresses many of the issues encountered in inversion, this approach greatly expands the parameter space, which makes inversion a highly under-determined problem. Having prior knowledge of the operators via constraints can help steer the updates and reduce the number of unknowns in the **W** operators.

CONCLUSIONS

We present an extension to the JMI method that takes into account VTI kinematics. We make use of the acoustic anisotropic dispersion relation associated with the acoustic wave-equation for VTI media. It enables us to describe the anisotropic kinematics without having to resort to full elastic modeling, which in turn greatly reduces the number of parameters needed for inversion. The artifacts associated with the acoustic anisotropic

dispersion relation were attenuated in a straightforward manner since we were using phase shift extrapolators.

Anisotropic JMI is based on integrating anisotropic velocity estimates with reflectivity estimates, thereby making the process of inversion robust. For a layered model, we evaluated the cost function for a number of different cases and different solutions. When the reflectivity is fixed the cost function oscillates, which increases the chance of getting stuck in a local minimum. Estimating the best fit reflectivity between each iteration of velocity updates drastically changes the shape of the cost function, making it less cyclic. Even when the discrepancy between the true and initial starting models is large the solution converges in an appropriate direction. This effect is demonstrated in the cost function analysis and with a synthetic example (example 1).

Addressing internal multiples during inversion not only reduces the imprint of the cross-talk in the image, but can introduce extra sensitivity in updating the velocities. The cost function shows that trade-off between the anisotropic parameters decreases when internal multiples are included. Internal multiples generally spend more time in the subsurface, therefore, they generally are more sensitive to the subsurface parameters. This in turn helps in uniquely defining the subsurface parameters and subsequently reduces the trade-off. For the second synthetic example, using internal multiples, we verify the extra sensitivity that internal multiples bring. We see that when multiples are present in the data and are ignored in the inversion, they produce erroneous images that prioritized focusing the internal multiples which causes erroneous anisotropic velocities. However, when they are properly addressed they produce an image that focused the primaries and generated suitable corresponding anisotropic velocity models. Finally, using the same model we generated only primaries in the observed data and proceeded to invert for the primaries-only. We note that

the trade-off is more significant in the inverted results, compared to the case where internal multiples were both present in the observed data and included in the inversion.

We then demonstrate the method on the HESS VTI model, where we estimated the reflectivity and anisotropic velocities. We find that the velocities correspond well to the true velocities while the reflectivity is a sharp, though band-limited, representation of the true reflectivity. Finally, the method is illustrated on a marine data set from the North Sea. The initial isotropic velocity produced an image with many unfocused and discontinuous reflectors. Furthermore, the associated ADCIGs were significantly curved (upward) indicating velocity errors. By applying anisotropic JMI we find the best fit anisotropic velocity model and the best fit reflectivity model. We note that the reflectivity is more continuous and the faults in the deep parts of the section are more visible. Analyzing the ADCIGs shows that the majority of the events have been flattened.

ACKNOWLEDGMENTS

The authors thank the sponsors of the Delphi consortium for their support. Abdulrahman Alshuhail thanks Saudi Aramco in particular for sponsoring his studies at TUDelft. We thank SEG, HESS, and ExxonMobil for providing the various synthetic and marine data sets. Finally we thank T. Alkhalifah and an anonymous reviewer for their constructive comments and suggestions.

APPENDIX A

Vertical Velocity Gradient

We linearize the propagation operator (equations 15 and 16) with respect to the contrast parameter β_v. Each element can be written in the wavenumber frequency domain as:

$$\frac{\partial}{\partial \beta_v}\left[\tilde{W}(k_x; z_{m+1}, z_{m+1}; \omega)\right]_{\beta_v=0} = -j\Delta z\left(e^{-jk_z\Delta z}e^{-jk_x x_i}\right)\frac{\partial}{\partial \beta_v}\left[k_z\right]_{\beta_v=0}. \tag{36}$$

where,

$$\frac{\partial}{\partial \beta_v}\left[k_z\right]_{\beta_v=0} = \frac{1}{2}\frac{1}{k_z}\frac{\partial}{\partial \beta_v}\left[\frac{\omega^2}{V_v^2} - \frac{\omega^2(1+2\delta)k_x^2}{\omega^2 - V_h^2k_x^2 + V_v^2(1+2\delta)k_x^2}\right]_{\beta_v=0} \tag{37}$$

Note that we are using the acoustic anisotropic dispersion relation to express k_z (equation 8). Taking the first expression and substituting the contrast parameter with velocities (equation 12) we arrive at,

$$\frac{\partial}{\partial \beta_v}\left[\frac{\omega^2}{V_v^2}\right]_{\beta_v=0} = \omega^2\frac{\partial}{\partial \beta_v}\left[\frac{1-\beta_v}{V0_v^2}\right]_{\beta_v=0} = \frac{-\omega^2}{V0_v^2}. \tag{38}$$

The second expression can be calculated by applying the quotient rule

$$\frac{f\left[\frac{\partial g}{\partial \beta_v}\right] - g\left[\frac{\partial f}{\partial \beta_v}\right]}{g^2}, \tag{39}$$

where

$$f = -\omega^2(1+2\delta)k_x^2, \tag{40a}$$

$$\begin{aligned}\left[\frac{\partial f}{\partial \beta_v}\right]_{\beta_v=0} &= \left[\frac{\partial\left(-\omega^2(1+2\delta)k_x^2\right)}{\partial \beta_v}\right]_{\beta_v=0} \\ &= 0,\end{aligned} \tag{40b}$$

$$g = \omega^2 - V_h^2k_x^2 + V_v^2(1+2\delta)k_x^2, \tag{40c}$$

$$\begin{aligned}\left[\frac{\partial g}{\partial \beta_v}\right]_{\beta_v=0} &= \left[\frac{\partial\left(\omega^2 - V_h^2 k_x^2 + V_v^2(1+2\delta)k_x^2\right)}{\partial \beta_v}\right]_{\beta_v=0} \\ &= 0 - 0 + (1+2\delta)k_x^2 \frac{\partial}{\partial \beta_v}\left[V_v^2\right]_{\beta_v=0} \\ &= V0_v^2(1+2\delta)k_x^2 \frac{\partial}{\partial \beta_v}\left[\frac{1}{1-\beta_v}\right]_{\beta_v=0} \\ &= V0_v^2(1+2\delta)k_x^2.\end{aligned} \tag{40d}$$

Hence,

$$\frac{\partial}{\partial \beta_v}\left[\frac{-\omega^2(1+2\delta)k_x^2}{\omega^2 - V_h^2 k_x^2 + V_v^2(1+2\delta)k_x^2}\right]_{\beta_v=0} = \frac{\omega^2 V0_v^2(1+2\delta)^2 k_x^4}{\left(\omega^2 - V_h^2 k_x^2 + V0_v^2(1+2\delta)k_x^2\right)^2}. \tag{41}$$

Finally, we can write the linearization of equation 36 as

$$\frac{\partial}{\partial \beta_v}\left[\tilde{W}\right]_{\beta_v=0} = \frac{-j\Delta z}{2k_z}\left(e^{-jk_z\Delta z}e^{-jk_x x_i}\right)\left(\frac{-\omega^2}{V0_v^2} + \frac{\omega^2 V0_v^2(1+2\delta)^2 k_x^4}{\left(\omega^2 - V_h^2 k_x^2 + V0_v^2(1+2\delta)k_x^2\right)^2}\right). \tag{42}$$

Horizontal Velocity Gradient

We also linearize the propagation operator (equations 27 and 28) with respect to β_h. Each element can be written in the wavenumber frequency domain as:

$$\frac{\partial}{\partial \beta_h}\left[\tilde{W}(k_x; z_{m+1}, z_{m+1}; \omega)\right]_{\beta_h=0} = -j\Delta z\left(e^{-jk_z\Delta z}e^{-jk_x x_i}\right)\frac{\partial}{\partial \beta_h}\left[k_z\right]_{\beta_h=0}, \tag{43}$$

where,

$$\frac{\partial}{\partial \beta_h}\left[k_z\right]_{\beta_h=0} = \frac{1}{2}\frac{1}{k_z}\frac{\partial}{\partial \beta_h}\left[\frac{\omega^2}{V_v^2} - \frac{\omega^2(1+2\delta)k_x^2}{\omega^2 - V_h^2 k_x^2 + V_v^2(1+2\delta)k_x^2}\right]_{\beta_h=0}. \tag{44}$$

Note that, as in the previous case, we are using the acoustic anisotropic dispersion relation to express k_z (equation 8). Taking the first expression we find that,

$$\frac{\partial}{\partial \beta_h}\left[\frac{\omega^2}{V_v^2}\right]_{\beta_h=0} = 0. \tag{45}$$

The second expression can be calculated by applying the quotient rule (equation 39), where

$$f = -\omega^2(1+2\delta)k_x^2, \tag{46a}$$

$$\begin{aligned}\left[\frac{\partial f}{\partial \beta_h}\right]_{\beta_h=0} &= \left[\frac{\partial\left(-\omega^2(1+2\delta)k_x^2\right)}{\partial \beta_h}\right]_{\beta_h=0} \\ &= 0,\end{aligned} \tag{46b}$$

$$g = \omega^2 - V_h^2 k_x^2 + V_v^2(1+2\delta)k_x^2, \tag{46c}$$

$$\begin{aligned}\left[\frac{\partial g}{\partial \beta_h}\right]_{\beta_h=0} &= \left[\frac{\partial\left(\omega^2 - V_h^2 k_x^2 + V_v^2(1+2\delta)k_x^2\right)}{\partial \beta_h}\right]_{\beta_h=0} \\ &= 0 - k_x^2 \frac{\partial}{\partial \beta_h}\left[V_h^2\right]_{\beta_h=0} + 0 \\ &= -V0_h^2 k_x^2 \frac{\partial}{\partial \beta_h}\left[\frac{1}{1-\beta_h}\right]_{\beta_h=0} \\ &= -V0_h^2 k_x^2.\end{aligned} \tag{46d}$$

Hence,

$$\frac{\partial}{\partial \beta_h}\left[\frac{-\omega^2(1+2\delta)k_x^2}{\omega^2 - V_h^2 k_x^2 + V_v^2(1+2\delta)k_x^2}\right]_{\beta_h=0} = \frac{-\omega^2 V0_h^2(1+2\delta)k_x^4}{\left(\omega^2 - V0_h^2 k_x^2 + V_v^2(1+2\delta)k_x^2\right)^2}. \tag{47}$$

Finally, we can write the linearization of equation 43 as

$$\frac{\partial}{\partial \beta_h}\left[\tilde{W}\right]_{\beta_h=0} = \frac{-j\Delta z}{2k_z}\left(e^{-jk_z\Delta z}e^{-jk_x x_i}\right)\left(\frac{-\omega^2 V0_h^2(1+2\delta)k_x^4}{\left(\omega^2 - V0_h^2 k_x^2 + V_v^2(1+2\delta)k_x^2\right)^2}\right). \tag{48}$$

REFERENCES

Aki, K., and P. G. Richards, 1980, Quantative seismology: W. H. Freeman and Co.

Al-Yahya, K. M., 1989, Velocity analysis by iterative profile migraton: Geophysics, **54**, 718–729.

Alkhalifah, T., 1997, Seismic data processing in vertically inhomogeneous TI media: Geophysics, **62**, 662–675.

———, 2000a, An acoustic wave equation for anisotropic media: Geophysics, **65**, 1239–1250.

———, 2000b, Prestack phase-shift migration of separate offsets: Geophysics, **65**, 1179–1194.

———, 2014, Full waveform inversion in an anisotropic world: EAGE Publications BV.

———, 2016, Research note: Insights into the data dependency on anisotropy: An inversion prospective: Geophysical Prospecting, **64**, 505–513.

———, 2017, Research note: The sensitivity of surface seismic Pwave data in transversely isotropic media to reflector depth: Geophysical Prospecting, **65**, 1398–1406.

Alkhalifah, T., and R. É. Plessix, 2014, A recipe for practical full-waveform inversion in anisotropic media: An analytical parameter resolution study: Geophysics, **79**, R91–R101.

Alkhalifah, T., and I. Tsvankin, 1995, Velocity analysis for transversely isotropic media: Geophysics, **60**, 1550–1566.

Alkhalifah, T., and Z. Wu, 2016, Multiscattering inversion for low-model wavenumbers: Geophysics, **81**, R417–R428.

Alshuhail, A., and D. J. Verschuur, 2015, Robust anisotropy estimation using joint migration inversion: 85th Ann. Internat. Mtg., SEG, Expanded Abstracts, Soc. Expl. Geophys., Expanded abstracts, 472–477.

Alshuhail, A. A., and D. J. Verschuur, 2014, Incorporating Anisotropy in Joint Migration Inversion: 84th Ann. Internat. Mtg., SEG, Expanded Abstracts, Soc. Expl. Geophys.,

Expanded abstracts, 415–419.

Anderson, J., T. Alkhalifah, and I. Tsvankin, 1996, Fowler DMO and time migration for transversely isotropic media: Geophysics, **61**, 835–845.

Bale, R. A., 2007, Phase-shift migration and the anisotropic acoustic wave equation: 66th Ann. Internat. Mtg., EAGE, Expanded Abstracts, Eur. Ass. of Geosc. and Eng., Expanded abstracts, C021.

Banik, N. C., 1984, Velocity anisotropy of shales and depth estimation in the North Sea basin: Geophysics, **49**, 1411–1419.

Berkhout, A. J., 1980, Seismic migration, imaging of acoustic energy by wave field extrapolation, vol. 14a: theoretical aspects: Elsevier; second edition in 1982 and third edition in 1985.

———, 2012, Combining full wavefield migration and full waveform inversion, a glance into the future of seismic processing: Geophysics, **77**, S43–S50.

———, 2014a, Review Paper: An outlook on the future of seismic imaging, Part I: forward and reverse modelling: Geophys. Prosp., **62**, 911–930.

———, 2014b, Review Paper: An outlook on the future of seismic imaging, Part II: Full-wavefield migration: Geophys. Prosp., **62**, 931–949.

———, 2014c, Review Paper: An outlook on the future of seismic imaging, Part III: Joint Migration Inversion: Geophys. Prosp., **62**, 950–971.

Berkhout, A. J., and D. J. Verschuur, 2016, Enriched seismic imaging by using multiple scattering: The Leading Edge, **35**, 128–133.

Berkhout, A. J., D. J. Verschuur, and X. R. Staal, 2015, Integration of velocity estimation and nonlinear migration: 85th Ann. Internat. Mtg., SEG, Expanded Abstracts, Soc. Expl. Geophys., Expanded abstracts, 5233–5237.

Bremmer, H., 1951, The WKB approximation as the first term of a geometric-optical series: Communications on Pure and Applied Mathematics, **4**, 105–115.

Bunks, C., S. M. Saleck, S. Zaleski, and G. Chavent, 1995, Multiscale seismic waveform inversion: Geophysics, **60**, 1457–1473.

Byun, B. S., D. Corrigan, and J. E. Gaiser, 1989, Anisotropic velocity analysis for lithology discrimination: Geophysics, **54**, 1564–1574.

Cheng, X., K. Jiao, D. Sun, and D. Vigh, 2014, Anisotropic parameter estimation with full-waveform inversion of surface seismic data: 84th Ann. Internat. Mtg., SEG, Expanded Abstracts, Soc. Expl. Geophys., Expanded abstracts, 1072–1076.

Davydenko, M., and D. J. Verschuur, 2013, Full wavefield migration, using internal multiples for undershooting: 83th Ann. Internat. Mtg., SEG, Expanded Abstracts, Soc. Expl. Geophys., Expanded abstracts, 3741–3745.

———, 2017a, Full-wavefield estimation of angle-dependent reflectivity and migration velocity: 87th Ann. Internat. Mtg., SEG, Expanded Abstracts, Soc. Expl. Geophys., Expanded abstracts, 5631–5635.

———, 2017b, Full-wavefield migration: using surface and internal multiples in imaging: Geophys. Prosp., **65**, 7–21.

de Hoop, M. V., J. H. L. Rousseau, and R. Wu, 2000, Generalization of the phase-screen approximation for the scattering of acoustic waves: Wave Motion, **31**, 43–70.

Gholami, Y., R. Brossier, S. Operto, V. Prieux, A. Ribodetti, and J. Virieux, 2013a, Which parameterization is suitable for acoustic vertical transverse isotropic full waveform inversion? Part 2: Synthetic and real data case studies from Valhall: Geophysics, **78**, R107–R124.

Gholami, Y., R. Brossier, S. Operto, A. Ribodetti, and J. Virieux, 2013b, Which param-

eterization is suitable for acoustic vertical transverse isotropic full waveform inversion? Part 1: Sensitivity and trade-off analysis: Geophysics, **78**, R81–R105.

Groenestijn, G. J. V., and D. J. Verschuur, 2009a, Estimating primaries by sparse inversion and application to near-offset data reconstruction: Geophysics, **74**, A23–A28.

———, 2009b, Estimation of primaries and near-offset reconstruction by sparse inversion: Marine data applications: Geophysics, **74**, R119–R128.

Han, B., T. Galikeev, V. Grechka, J. L. Rousseau, and I. Tsvankin, 2000, A synthetic example of anisotropic P-wave processing for a model from the Gulf of Mexico: Presented at the Anisotropy 2000: Fractures, converted waves and case studies: Proceedings of the 9th International Workshop on Seismic Anisotropy (9IWSA), SEG, Soc. Expl. Geophys.

Kabir, M. M. N., and D. J. Verschuur, 1995, Restoration of missing offsets by parabolic radon transform: Geophys. Prosp., **43**, 347–368.

Keys, R. G., and D. J. Foster, 1998, Comparison of sesimic inversion methods on a single real data set: Society of Exploration Geophysicists.

Kumar, A., G. Blacquière, and D. J. Verschuur, 2014, 3-D acquisition geometry analysis: incorporating information from multiples: 84th Ann. Internat. Mtg., SEG, Expanded Abstracts, Soc. Expl. Geophys., Expanded abstracts, 30–35.

Lee, H. Y., J. M. Koo, D. J. Min, B. D. Kwon, and H. S. Yoo, 2010, Frequency-domain elastic full waveform inversion for VTI media: Geophys. J. Int., **183**, 884–904.

Levin, F., 1979, Seismic velocities in transversely isotropic media: Geophysics, **44**, 918–936.

Li, V., H. Wang, I. Tsvankin, E. Díaz, and T. Alkhalifah, 2017, Inversion gradients for acoustic VTI wavefield tomography: Geophysics, **82**, WA55–WA65.

Li, Y., and B. Biondi, 2011, Migration velocity analysis for anisotropic models: 81st Ann. Internat. Mtg., SEG, Expanded Abstracts, Soc. Expl. Geophys., Expanded abstracts,

201–206.

Lu, S., A. A. Valenciano, N. Cheminigui, and D. B. Lecerf, 2015, Separated Wavefield Imaging of Ocean Bottom Seismic (OBS) Data: 77th Ann. Internat. Mtg., EAGE, Expanded Abstracts, Eur. Ass. of Geosc. and Eng., Expanded abstracts, WeN10608.

Lynn, W., A. Gonzalez, and S. MacKay, 1991, Where are the fault-plane reflections?: 61st Ann. Internat. Mtg., SEG, Expanded Abstracts, Soc. Expl. Geophys., Expanded abstracts, 1151–1154.

Marhfoul, B. E., and D. J. Verschuur, 2016, High-resolution, integrated 3D joint migration inversion of surface and VSP data: 86th Ann. Internat. Mtg., SEG, Expanded Abstracts, Soc. Expl. Geophys., Expanded abstracts, 672–676.

Plessix, R. É., and Q. Cao, 2010, A parametrization study for surface seismic full waveform inversion in an acoustic vertical transversely isotropic medium: Geophys. J. Int., **185**, 539–556.

Plessix, R. É., and C. Perkins, 2010, Full waveform inversion of a deep water ocean bottom seismometer dataset: First Break, **28**, 71–78.

Pratt, R. G., 1999, Seismic waveform inversion in the frequency domain, part 1: Theory and verification in a physical scale model: Geophysics, **64**, 888–901.

Robein, E., 2003, Velocities, time-imaging and depth imaging: Principles and methods: EAGE Publications BV.

Staal, X. R., and D. J. Verschuur, 2012, Velocity estimation using internal multiples: 82nd Ann. Internat. Mtg., SEG, Expanded Abstracts, Soc. Expl. Geophys., Expanded abstracts, 1–5.

———, 2013, Joint migration inversion, imaging including all multiples with automatic velocity update: 75th Ann. Internat. Mtg., EAGE, Expanded Abstracts, Eur. Ass. of Geosc.

and Eng., Expanded abstracts, Tu0216.

Staal, X. R., D. J. Verschuur, and A. J. Berkhout, 2014, Robust velocity estimation by joint migration inversion: 76th Ann. Internat. Mtg., EAGE, Expanded Abstracts, Eur. Ass. of Geosc. and Eng., Expanded abstracts, WeG10307.

Symes, W. W., and J. J. Carazzone, 1991, Velocity inversion by differential semblance optimization: Geophysics, **56**, 654–663.

Symes, W. W., and M. Kern, 1994, Inversion of reflection seismograms by differential semblance analysis: Algorithm structure and synthetic examples: Geophysical Prospecting, **42**, 565–614.

Tarantola, A., 1987, Inverse problem theory, methods for data fitting and model parameter estimation: Elsevier Science Publ. Co., Inc.

Thomsen, L., 1986, Weak elastic anisotropy: Geophysics, **51**, 1954–1966.

Tsvankin, I., J. Gaiser, V. Grechka, M. van der Baan, and L. Thomsen, 2010, Seismic anisotropy in exploration and reservoir characterization: An overview: Geophysics, **75**, 75A15–75A29.

Verschuur, D. J., 2006, Seismic multiple removal techniques - past, present and future: EAGE Publications BV.

Verschuur, D. J., A. J. Berkhout, and C. P. A. Wapenaar, 1992, Adaptive surface-related multiple elimination: Geophysics, **57**, 1166–1177.

Verschuur, D. J., X. R. Staal, and A. J. Berkhout, 2016, Joint migration inversion: Simultaneous determination of velocity fields and depth images using all orders of scattering: The Leading Edge, **35**, 1037–1046.

Virieux, J., and S. Operto, 2009, An overview of full-waveform inversion in exploration geophysics: Geophysics, **74**, WCC1–WCC26.

Wapenaar, C. P. A., 1996, One-way representations of seismic data: Geophysical Journal International, **127**, 178–188.

Wapenaar, C. P. A., and A. J. Berkhout, 1989, Elastic wave field extrapolation: redatuming of single- and multi-component seismic data: Elsevier Science Publ. Co., Inc.

Weibull, W. W., and B. Arntsen, 2014, Anisotropic migration velocity analysis using reverse-time migration: Geophysics, **79**, R13–R25.

Whitmore, N. D., A. A. Valenciano, W. Sollner, and S. Lu, 2010, Imaging of primaries and multiples using a dual-sensor towed streamer: 80th Ann. Internat. Mtg., SEG, Expanded Abstracts, Soc. Expl. Geophys., Expanded abstracts, 3187–3192.

Zhang, D., and G. T. Schuster, 2013, Least-squares reverse time migration of multiples: Geophysics, **79**, S11–S21.

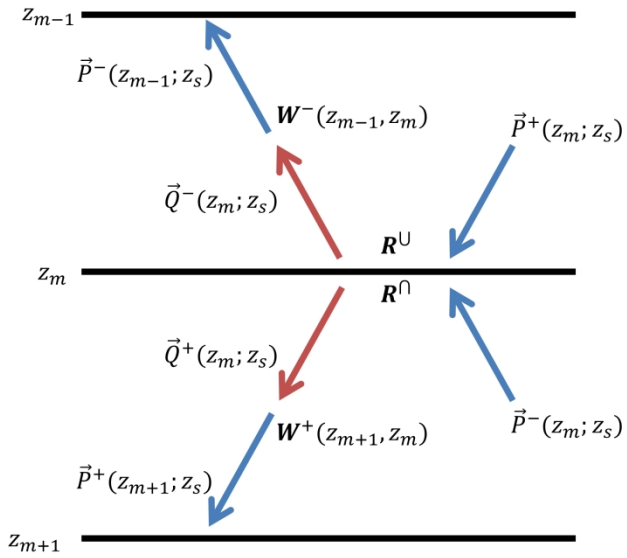

Figure 1: Schematic representation of the incoming and outgoing wavefields acting on a scattering depth level z_m.

254x190mm (300 x 300 DPI)

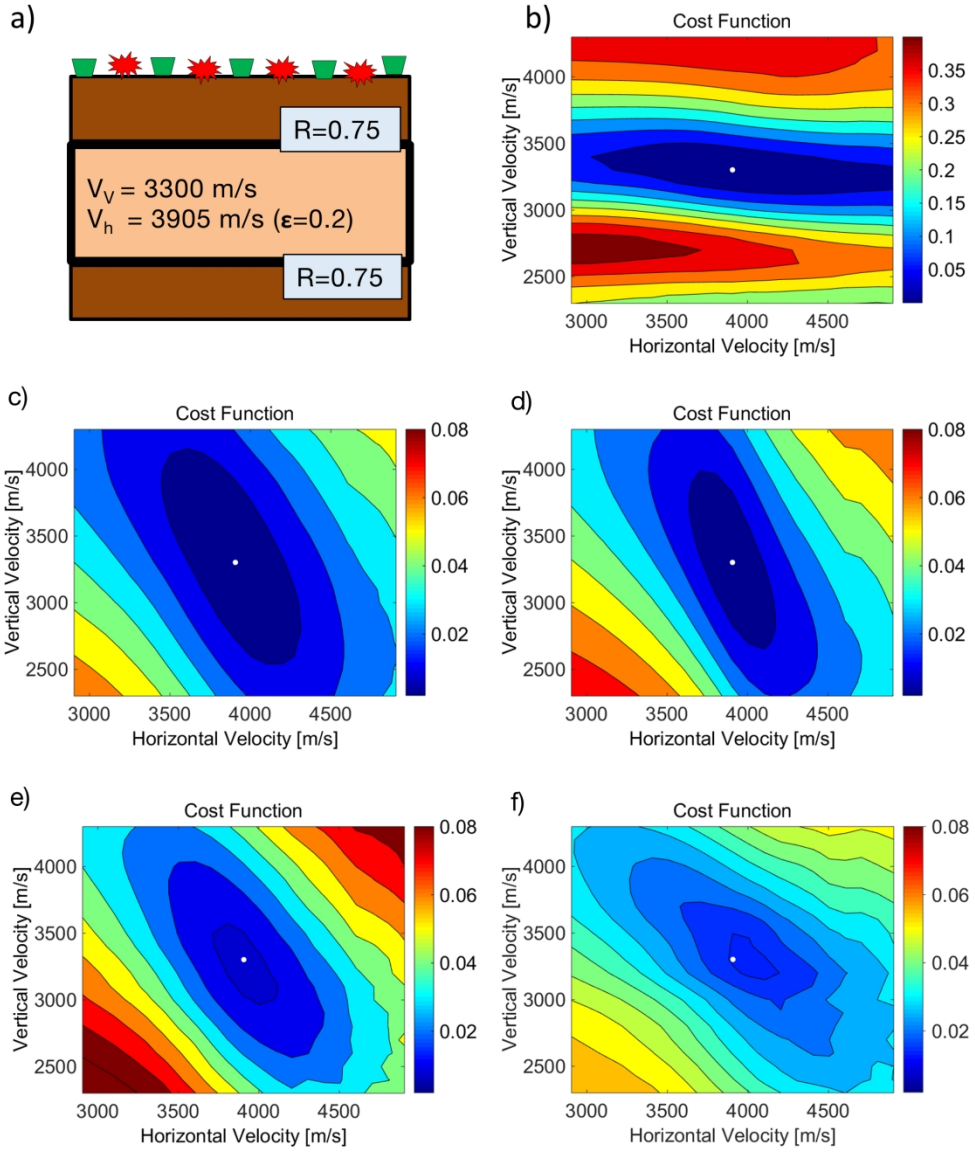

Figure 2: A synthetic example including a) a layered VTI model, b) the cost function when the reflectivity is fixed, c) The cost function when the reflectivity is estimated, d) the cost function when the offset is doubled, e) the cost function when both primaries and multiples are included, and f) the cost function when only internal multiples are considered.

190x226mm (300 x 300 DPI)

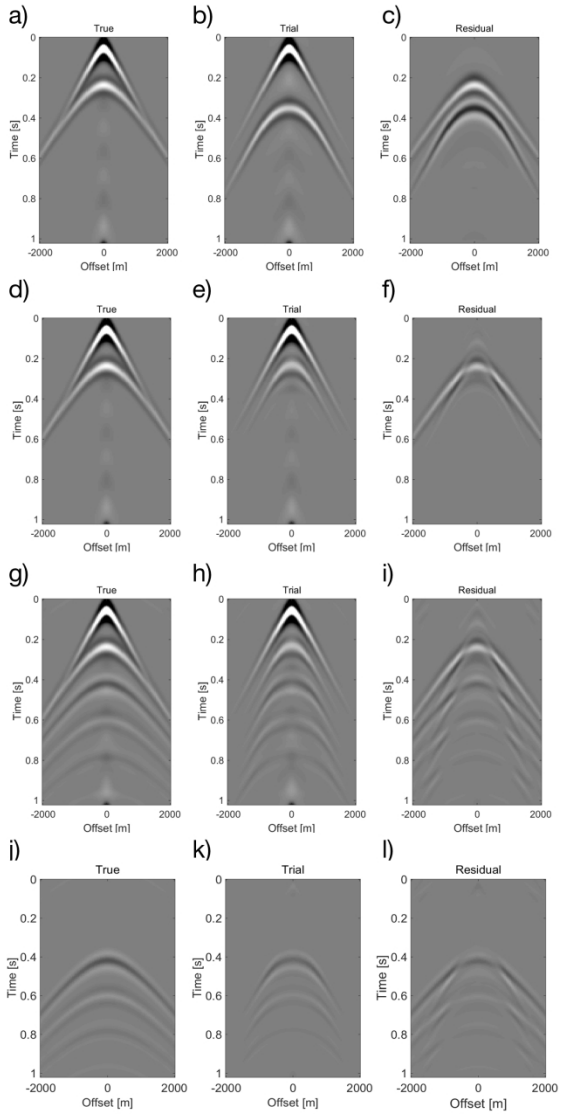

Figure 3: Included a) an input gather associated with the true model (Figure 2a), b) modeled gather using the trial velocities of V_v=2300m/s and V_h=2905m/s for a fixed reflectivity. c) difference between a) and b), d) an input gather e) modeled gather using the same trial velocities when the reflectivity is estimated, f) the difference between d) and e), g) an input gather including internal multiples, h) the modeled gather using trial velocities where reflectivity is estimated, and i) the difference between g) and h), j) an input gather including only internal multiples, k) the modeled internal multiples using the trial velocities, and l) the difference between j) and k).

190x275mm (300 x 300 DPI)

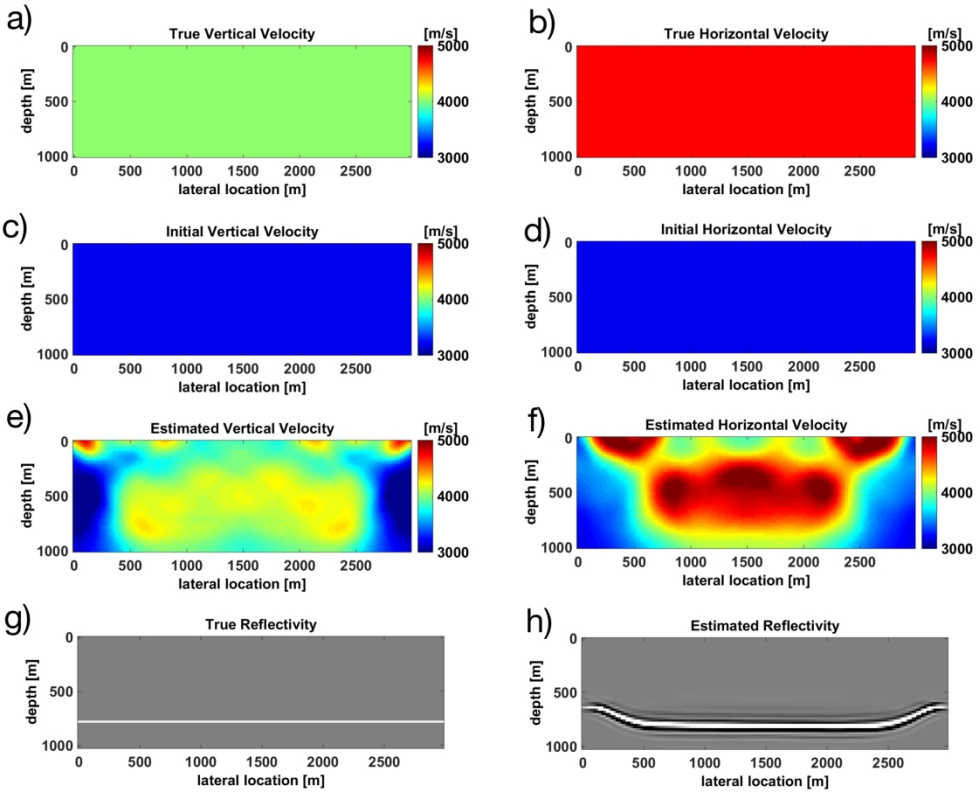

Figure 4: A synthetic example comprising a homogenous anisotropic model including a) the true vertical velocity V_v [m/s], b) the true horizontal velocity V_h [m/s], c) the initial vertical velocity V_v [m/s], d) the initial horizontal velocity V_h [m/s], e) the estimated vertical velocity V_v [m/s], f) the estimated horizontal velocity V_h [m/s], g) the true reflectivity, and h) the estimated reflectivity.

190x173mm (300 x 300 DPI)

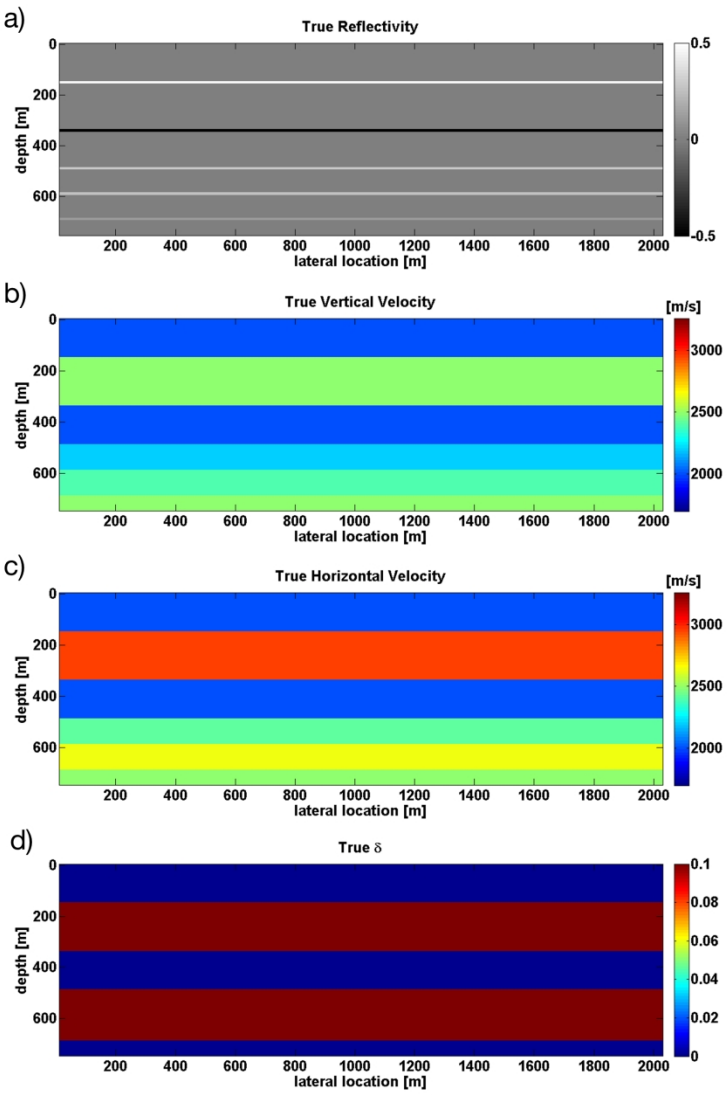

Figure 5: A synthetic example comprising a layered model for generating primaries and internal multiples including a) the reflectivity, b) the vertical velocity V_v [m/s], c) the horizontal velocity V_h [m/s], and d) the δ values.

190x275mm (300 x 300 DPI)

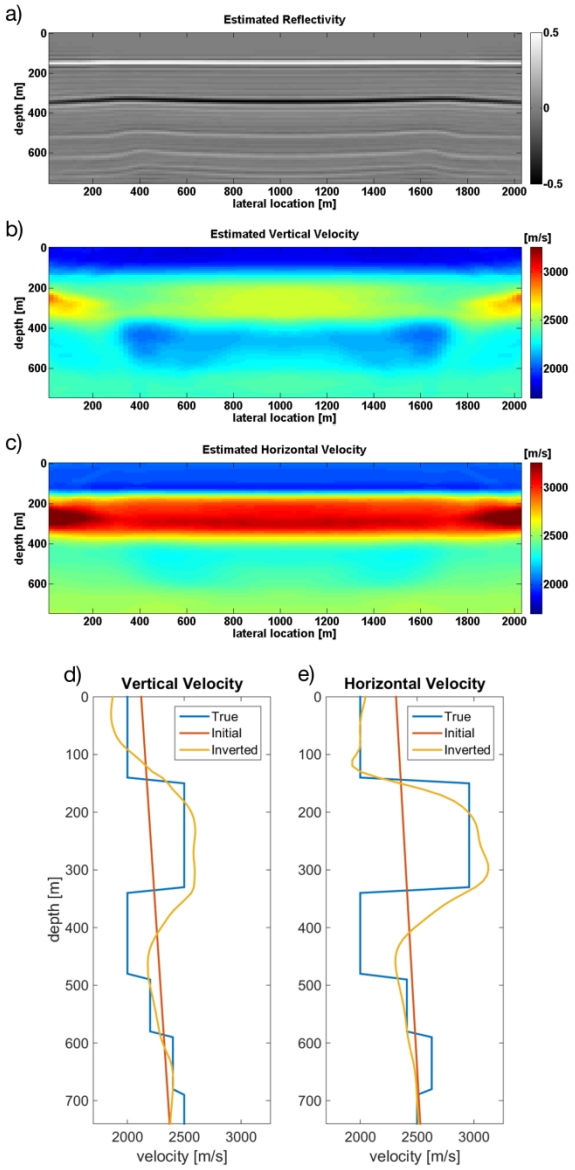

Figure 6: Inverted values from the internal multiple model when primaries and multiples are in the observed data and both are inverted including a) the reflectivity, b) the vertical velocity V_v [m/s], c) the horizontal velocity V_h [m/s], d) the log profile of V_v at 1010m, and e) the log profile of V_h at 1010m.

190x351mm (300 x 300 DPI)

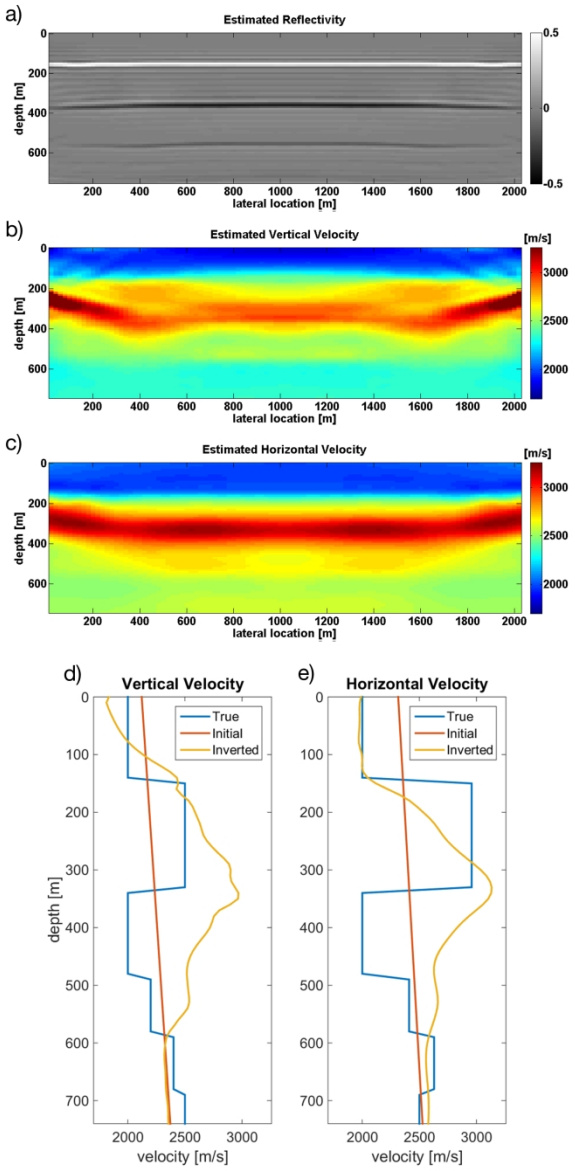

Figure 7: Inverted values from the internal multiple model when primaries and multiples are in the observed data and only primaries are inverted including a) the reflectivity, b) the vertical velocity V_v [m/s], c) the horizontal velocity V_h [m/s], d) the log profile of V_v at 1010m, and e) the log profile of V_h at 1010m.

190x351mm (300 x 300 DPI)

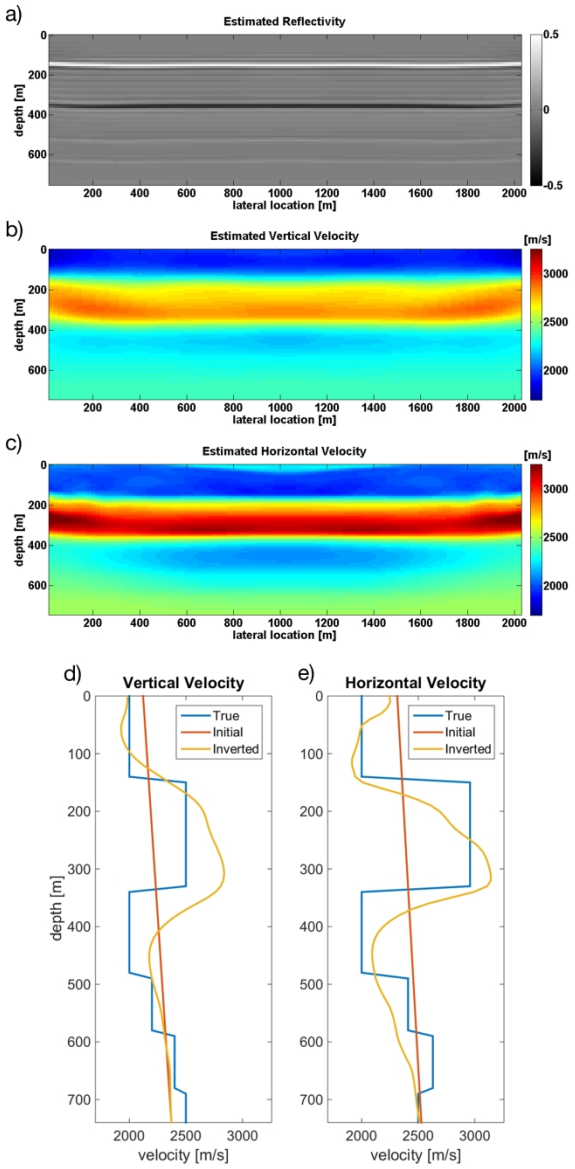

Figure 8: Inverted values from the internal multiple model when only primaries are in the observed data and only primaries are inverted (i.e., no internal multiples in the data) including a) the reflectivity, b) the vertical velocity V_v [m/s], c) the horizontal velocity V_h [m/s], d) the log profile of V_v at 1010m, and e) the log profile of V_h at 1010m.

190x351mm (300 x 300 DPI)

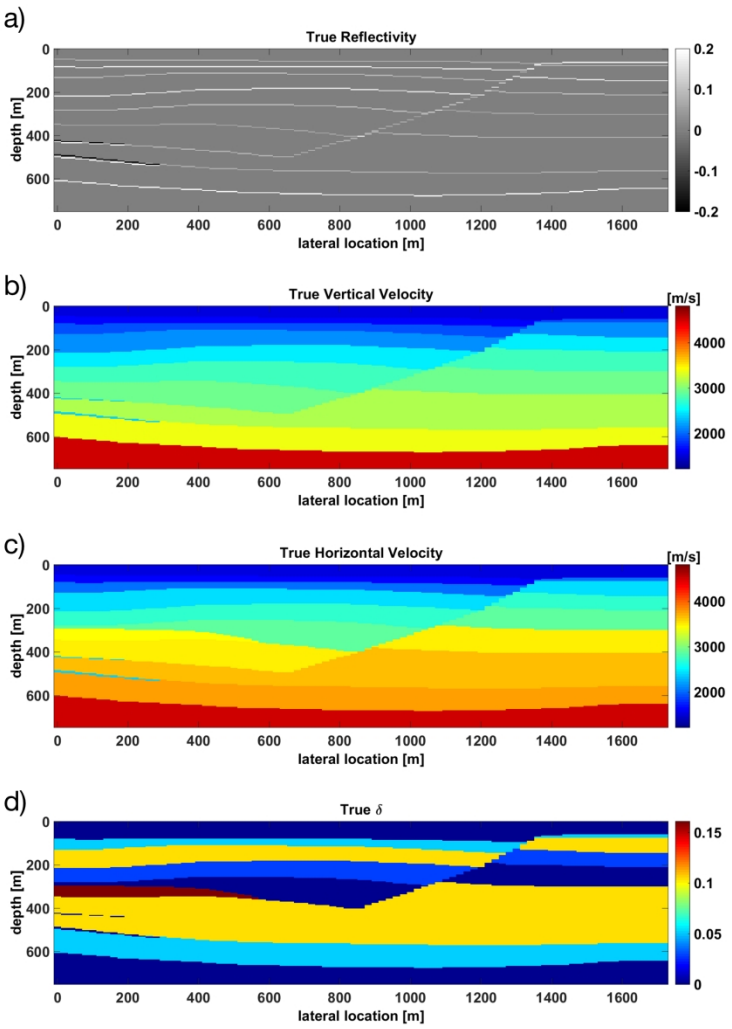

Figure 9: A synthetic example comprising of a subset of the HESS VTI model including a) the reflectivity, b) the vertical velocity V_v [m/s], c) the horizontal velocity V_h [m/s], and d) the δ values.

190x275mm (300 x 300 DPI)

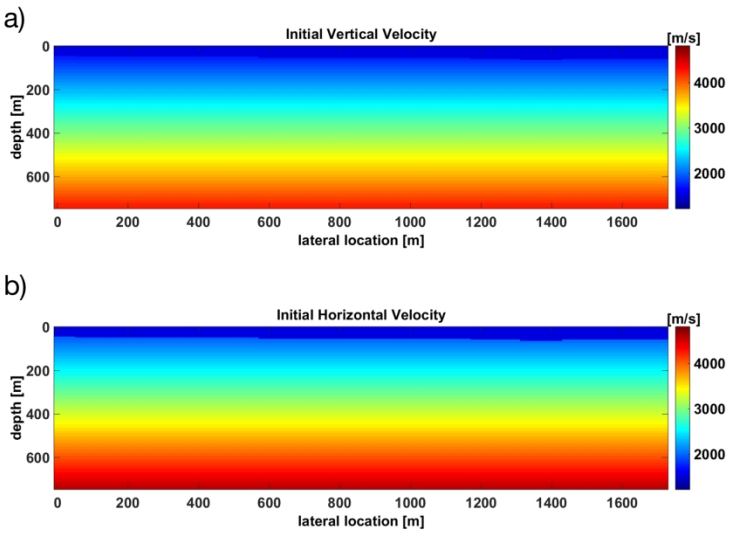

Figure 10: The initial values used for inversion including a) the vertical velocity V_v [m/s] and b) the horizontal velocity V_h [m/s].

190x275mm (300 x 300 DPI)

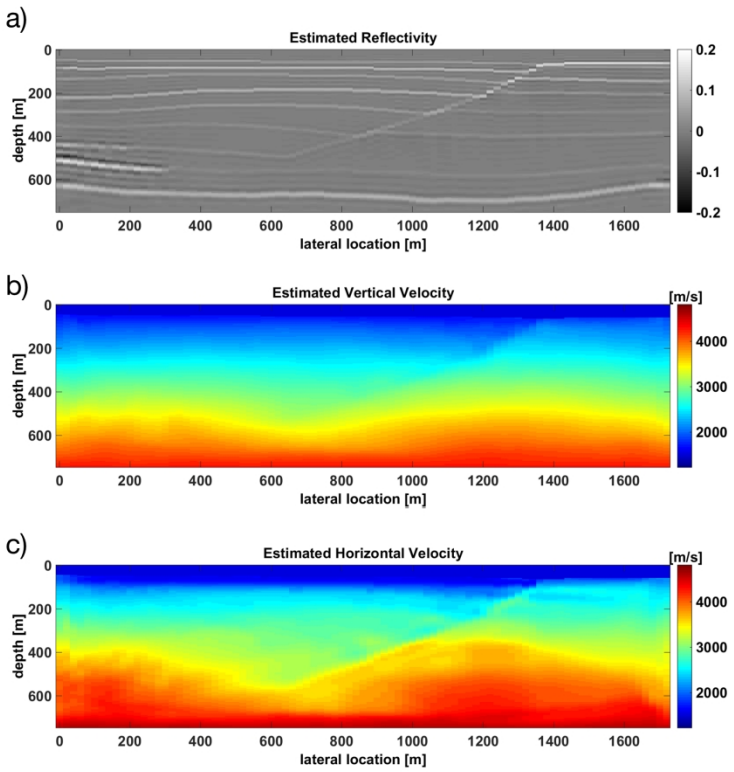

Figure 11: The inverted values for the HESS VTI model including a) the reflectivity, b) the vertical velocity V_v [m/s], and c) the horizontal velocity V_h [m/s].

190x275mm (300 x 300 DPI)

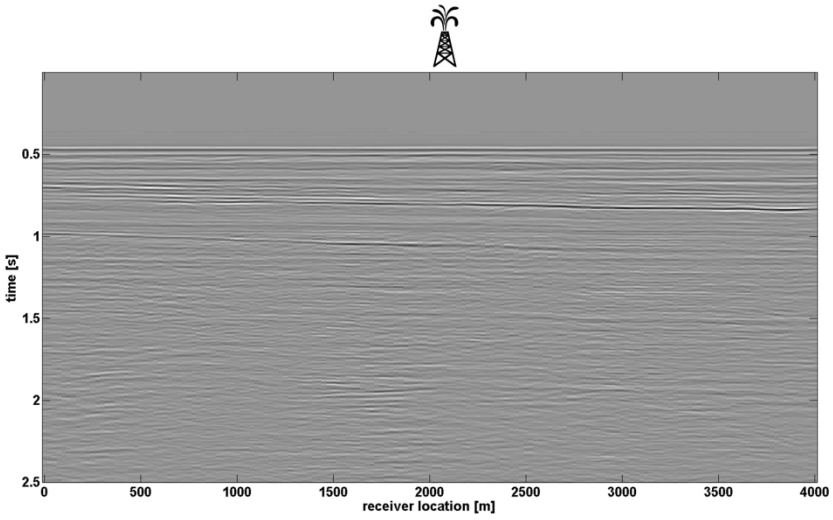

Figure 12: Zero-offset section of the marine data.

190x190mm (300 x 300 DPI)

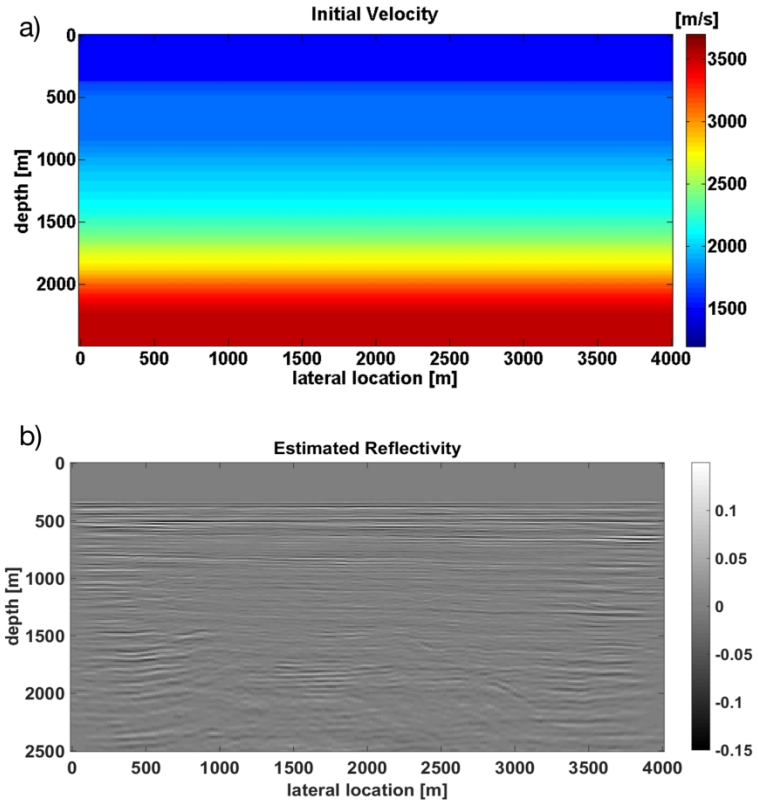

Figure 13: Marine data model showing a) initial values for the isotropic velocity [m/s] and b) the FWM image obtained via the isotropic initial velocity model.

190x275mm (300 x 300 DPI)

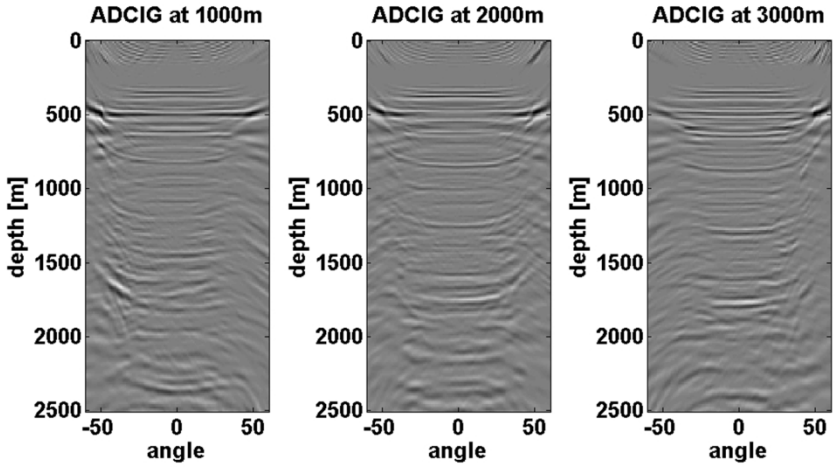

Figure 14: ADCIGs associated with the initial marine model at lateral locations of 1000m, 2000m, and 3000m.

190x152mm (300 x 300 DPI)

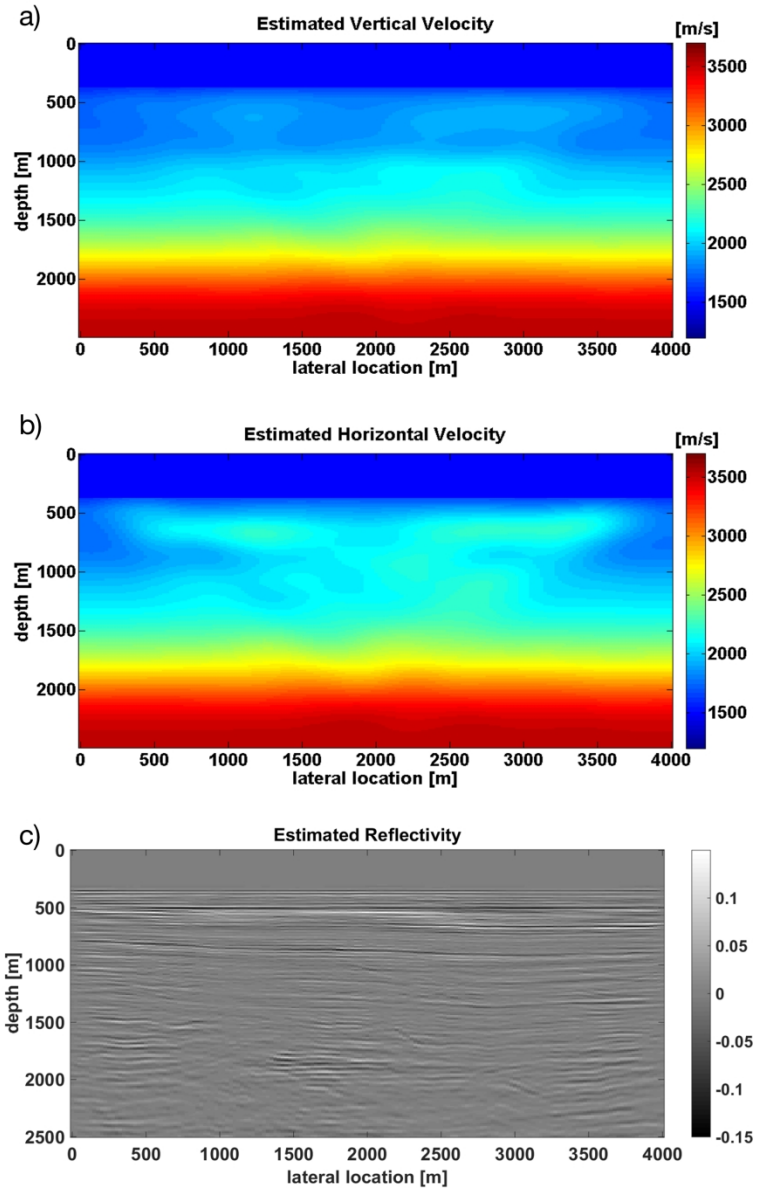

Figure 15: Inverted values for the marine data including a) the vertical velocity V_v [m/s], b) the horizontal velocity V_h [m/s], and c) the reflectivity.

190x275mm (300 x 300 DPI)

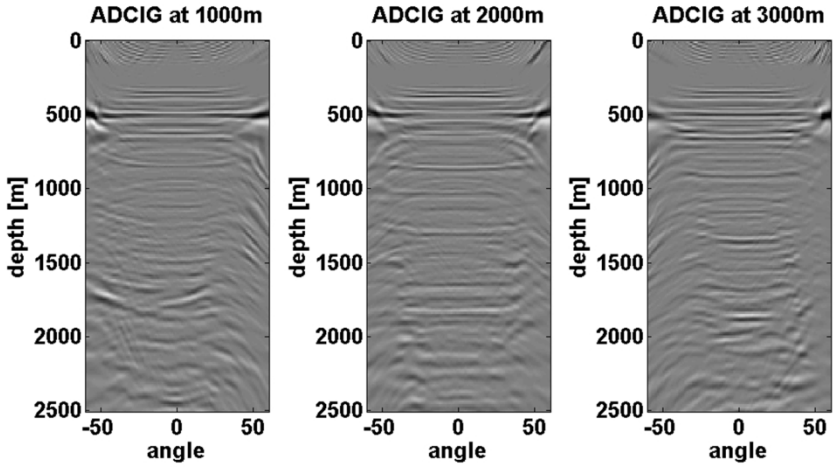

Figure 16: ADCIGs associated with the inverted anisotropic model (Figure 15) at lateral locations of 1000m, 2000m, and 3000m.

190x152mm (300 x 300 DPI)

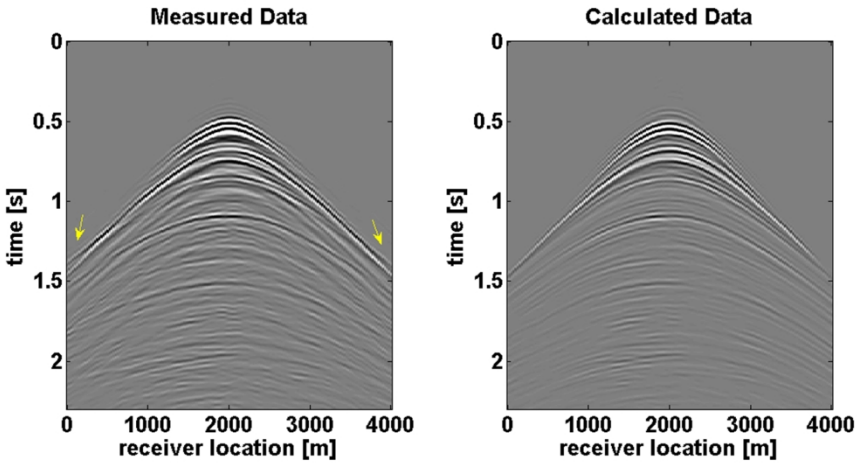

Figure 17: The measured and calculated data at 2000m for the marine data.

190x152mm (300 x 300 DPI)

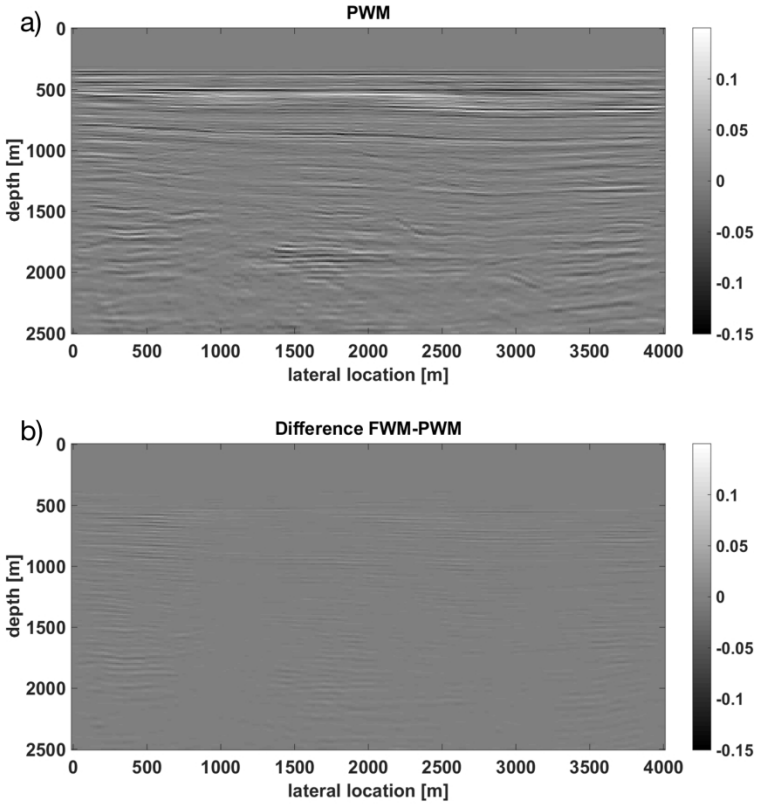

Figure 18: The marine data example showing a) the estimated image using primaries only PWM, and b) the difference between the PWM image (Figure 18a) and the FWM image (Figure 15c).

190x275mm (300 x 300 DPI)

Table 1:

Mean Percentage Difference		
	V_v	V_h
Observed: Primaries and multiples Inverted: Primaries and multiples	5.97%	7.66%
Observed: Primaries Inverted: Primaries	7.49%	8.51%
Observed: Primaries and multiples Inverted: Primaries	13.38%	12.99%

DATA AND MATERIALS AVAILABILITY

Data associated with this research are available and can be obtained by contacting the corresponding author.